We prepared the red cell ghosts according to the hypotonic lysis methods of Dodge et al. [17] from the blood drawn from healthy volunteers into syringes containing 3.8% sodium citrate solution. After the blood was processed by the procedure of a hypotonic lysis method, the hematocrit was adjusted to 40% with PBS.

Image analysis

To determine the concentration profiles, 1,500 images were taken by a data acquisition rate of 200 Hz for a shear rate of 190 s^{-1} and at 1,000 Hz for 1,500 s^{-1} by the high-speed camera. Then we tracked the trajectory of the particles by these sequential images and determined the concentration profile and velocity vectors with the axial and lateral component being normal to the axial direction based on 400 images. This image analysis was processed by NIH Image (National Institutes of Health, USA).

Results

Concentration profile of poly Alb particles in the duct

The half width of the flow duct was divided into ten segments with the thickness of 10 μm, where the number of particles was counted from 150 images. Thereby the concentration profile was determined, which is shown in Fig. 3. The abscissa is the distance from the center axis divided by the half width ($y = y^*/a$), namely $y = 0$ and $y = 1$ correspond to the center axis and the wall surface, respectively. The ordinate is the percentage expression of poly Alb number based on cumulative count.

Figure 3 shows the concentration profiles of large poly Alb at the higher and lower shear rate. We should note that the maximum concentration appeared at $y = 0.95$ at the wall shear rate of 1,500 s^{-1}, and the concentration was in excess near the wall, which was observed for the profile of natural platelets [10]. The maximum concentration at $y = 0.95$ was 33.8%. The profile for the lower shear rate of 190 s^{-1} tends to increase near the wall, although the maximum concentration at $y = 0.95$ is 20%.

Migration angle Φ of the flowing particle

The random motion of the particle occurs in the stochastic process, and we need to have a probability distribution to understand the particle motion. The parameter of random lateral motion is given by the migration angle, being defined as the angle of poly Alb velocity vector direction from the axial direction, which is given by the following.

$$\Phi = \tan^{-1}(V_{\text{lateral}}/V_{\text{axial}}) \quad (2)$$

Here we determined both the lateral and axial poly Alb velocity component by the displacement of particles during the fixed duration and then discussed the lateral motion of poly Alb based on the histogram of migration angle.

Figure 4 shows the poly Alb number as a function of the migration angle, indicating the histogram of migration angle Φ of large poly Alb flowing in the rectangular duct at the shear rate of 190 s^{-1}. The shape of the histogram indicates the statistical characteristics of particle motion, namely the peaked profile indicates less lateral motion, and the widely spread shape indicates more back and forward motion in the y direction. The migration angle profile near the center ($0.4 < y < 0.6$) is significantly peaked, suggesting that most of the poly Alb velocity vector directions are within ±9°. The profile in the middle ($0.6 < y < 0.8$) is close to that of the center. However, the range of migration angle near the wall shows a distinct difference from those

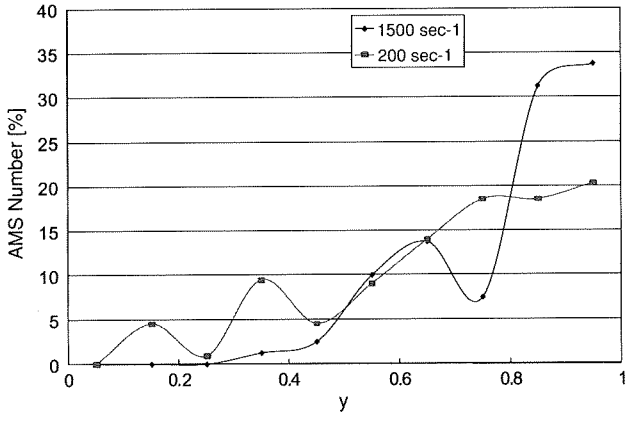

Fig. 3 Concentration profile of *r*GPIbα-poly Alb. Effect of wall shear rate on profiles of *r*GPIbα-poly Alb (diameter = 1.9 ± 0.4 μm). The near-wall excess (NWE) was clearly observed at 1,500 s^{-1}

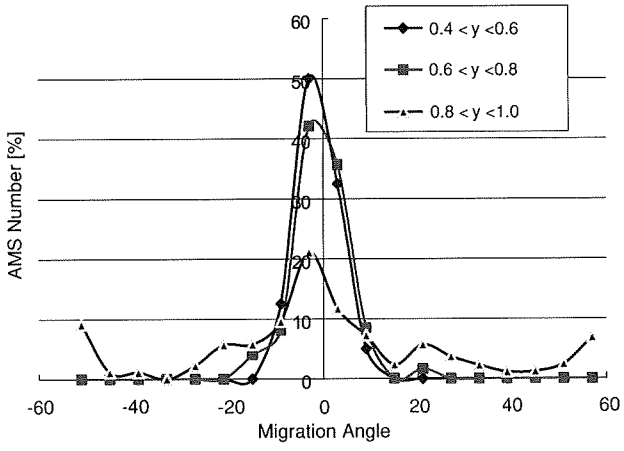

Fig. 4 Distribution of migration angle Φ of particle at three segments from the wall at shear rate 190 s^{-1}. *y* is the normalized *y** coordinate defined by (*y**/a), and the position of $y = 1$ is the wall surface

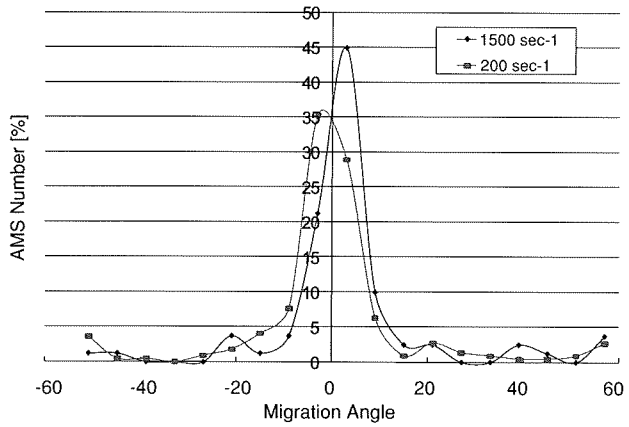

Fig. 5 Distribution of migration angle Φ of particle at high and low shear rate

of the center and exhibits the widely spread profile. The occurrence of a migration angle of 3° decreases to 40% of that near the center, and the maximum migration angle increases up to 51°, although the occurrence is low. This tendency is clearly indicated by the standard deviation of the migration angle. The standard deviation near the center is 4.16°, but becomes 21.2° near the wall. In Fig. 4, all of the profiles appear to be close to the Gaussian profile, but the standard deviation is changing. This shows an interesting feature of poly Alb particle motion, and the particles near the wall have a higher possibility to interact with the wall. This is a desirable feature for a platelet substitute.

Figure 5 shows the histograms of migration angle for higher and lower shear rates and shows a difference between them. We should note that the histogram profile for large shear rate shifts to the positive angle, indicating that particles tend to move toward the wall.

Discussion

Nonuniform distribution of natural and artificial platelets

Previous in vivo [10] and in vitro [18] studies have recognized the nonuniform concentration profiles with near wall excess (NWE) of platelets. They also noted that the red blood cells are necessary for the NWE profile. Eckstein et al. [18] showed that the NWE is related to biorheological conditions such as the wall shear rate or hematocrit. They reported that the NWE of platelet-sized beads occurred when the hematocrit was 7% or more and the shear rate was above 430 s^{-1}. On the other hand, the platelet substitute of *r*GPIbα-poly Alb with the diameter of 2 μm used in this study showed the NWE in the presence of the red cell ghosts Hct 40% at a higher shear rate of 1,500 s^{-1}. This is a desirable feature for artificial platelets because NWE will promote the interaction with the wall for the artificial platelets, as recognized for natural platelets. Eckstein et al. [18] also noted that the particles with a diameter less than 1 μm do not form a remarkable profile of NWE.

The interaction between the particles

The blood is a concentrated RBC suspension with platelets and white blood cells, and the interaction between the cells is dominant. The interaction depends on the collision, adhesive force of glycoprotein, the colloidal electrostatic repulsion and the van der Waals attraction forces. As a result, red blood cells show an erratic random displacement in a direction normal for the axial direction [12]. At the same time, the platelets collide with red blood cells and the platelets themselves. This interaction plays an essential role for the platelet aggregation formation. The fluctuation of poly Alb comes possibly from the progressive multibody collisions depending on the cell concentration, velocity gradients and deformation. Particularly we should note that poly Alb particles have a highly flexible property, which characterizes the interaction between red blood cells and poly Alb particles. Thus, we need to describe the amount of poly Alb fluctuation, which becomes a criterion for the interaction rate in the flow.

Migration angle Φ representing the motion of particles

To evaluate the motion of platelets, we need to have a parameter representing the motion of platelets. Here we defined the migration angle Φ to indicate a deviation of poly Alb particle motion from the axial direction. If the histogram of Φ was sharply peaked around the zero degree, the particle was moving straight in the axial direction and the particle did not interact with the other particles. If the histogram of the migration angle was flattened, a particle would increase the interaction rate, enhancing the adhesion to the wall surface and the formation of aggregation with other particles. The result of Fig. 4 shows an important implication of the interaction of particles near the wall. The standard deviation of the migration angle increased near the wall $0.8 < y < 1.0$.

Shear dependency of the migration angle

As shown in Fig. 5, poly Alb particle fluctuation velocity is enhanced at a higher shear rate. The microscopic motion of particulate in shear flow has physical and physiological implications. Particularly we should note that the particle lateral motion is augmented by sheared RBC suspensions. The overall transport of particulate is referred to as "convection-diffusion transport" [19]. The platelet transport is

interpreted by the effective platelet dispersivity [20]. The large fluctuation at a high shear rate contributes to increasing the poly Alb particle transport rate. This is a shear-induced transport of poly Alb particles toward the wall surface. Many previous studies dealt with shear-induced transport, such as that of oxygen and solute [21, 22]. On the other hand, the adhesive force between VWF and GPIbα increases with the increase of shear rate due to the conformational change of VWF molecules [23]. Thus, the nature of the shear-induced poly Alb particle transport and shear dependence of VWF is a key factor of the biorheological property of a platelet substitute.

Summary

The concentration profile of *r*GPIbα-poly Alb tends to peak near the wall. This profile enhances the interaction between particles and the wall. Particularly the migration angle of poly Alb particle velocity vector is enlarged near the wall and contributes to the transfer of the poly Alb particles toward the ligand-coating surface. This tendency is desirable to achieve the adhesion of particles on the ligand-immobilized surface.

Acknowledgments This work was supported by Health Science Research Grants (Artificial Platelets), Research on Advanced Medical Technology, Ministry of Health and Welfare, Japan.

References

1. Coller BS. Interaction of normal thrombasthetic and Bernard-Soulier platelets with immobilized fibrinogen: defective platelet-fibrinogen interaction in thrombasthenia. Blood. 1980;55:169–78.
2. George JN. Changes in platelet membrane glycoprotein during blood bank storage. Blood Cells. 1992;18:501–11.
3. Eaton LA, Read MS, Brinkhous KM. Glycoprotein Ib assays. Activity levels in Bernard-Soulier syndrome and in stored blood bank platelets. Arch Pathol Lab Med. 1991;115:488–93.
4. Kickler TS. Improving the quality of stored platelets. Transfusion. 1991;31:1–3.
5. Agam G, Livne A. Passive participation of fixed platelets in aggregation facilitated by covalently bound fibrinogen. Blood. 1983;61(1):186–91.
6. Agam G, Livne A. Erythrocytes with covalently bound fibrinogen as a cellular replacement for the treatment of thrombocytopenia. Eur J Clin Invest. 1992;22(2):105–12.
7. Murata M, Ware J, Ruggeri ZM. Site-directed mutagenesis of a soluble fragment of platelet glycoprotein Ibα demonstrating negatively charged residues involved in von Willebrand factor binding. J Biol Chem. 1991;266:15474–80.
8. Kitaguchi T, Murata M, Iijima K, Kamide K, Imagawa T, Ikeda Y. Characterization of liposomes carrying von Willebrand factor-binding domain of platelet glycoprotein Ibalpha: a potential substitute for platelet transfusion. Biochem Biophys Res Commun. 1999;261(3):784–9.
9. Takeoka S, Teramura Y, Ohkawa H, Ikeda Y, Tsuchida E. Conjugation of von Willebrand factor-binding domain of platelet glycoprotein Ibα to size-controlled albumin microspheres. Biomacromolecules. 2000;1(2):290–5.
10. Tangelder GJ, Teirlinck HC, Slaaf DW, Reneman RS. Distribution of blood platelets flowing in arterioles. Am J Physiol. 1985;248(3 Pt 2):H318–23.
11. Tilles AW, Eckstein EC. The near wall excess of platelet-sized particles in blood flow: its dependence on hematocrit and wall shear rate. Microvasc Res. 1987;33(2):211–23.
12. Goldsmith HL, Turitto VT. Rheological aspects of thrombosis and haemotstasis: basic principles and application. Thromb Haemost. 1986;55(3):415–35.
13. Nishiya T, Murata M, Handa M, Ikeda Y. Targeting of liposomes carrying recombinant fragments of platelet membrane glycoprotein Ibα to immobilized von Willebrand factor under flow conditions. Biochem Biophys Res Commun. 2000;270:755–60.
14. White FM. Viscous fluid flow. New York: McGraw-Hill; 1974. p. 123.
15. Goldsmith HL, Marlow JC. Flow behavior of erythrocytes. J Colloid Interface Sci. 1979;71(2):383–407.
16. Aarts PA, van den Broek SA, Prins GW, Kuiken GD, Sixma JJ, Heethaar RM. Blood platelets are concentrated near the wall and red blood cells, in the center in flowing blood. Arteriosclerosis. 1988;8(6):819–24.
17. Dodge JT, Mitchell C, Hanahan DJ. The preparation and chemical characteristics of hemoglobin-free ghosts of human erythrocytes. Arch Biochem Biophys. 1962;100:119.
18. Eckstein EC, Tilles AW, Millero FJD. Conditions for the occurrence of large near-wall excesses of small particles during blood flow. Microvasc Res. 1988;36(1):31–9.
19. Wang SK, Hwang NHC. On transport of suspended particulates in tube flow. Biorheology. 1992;29:353–77.
20. Goldsmith HL. Red cell motions and wall interactions in tube flow. Fed Proc. 1971;30(5):1578–88.
21. Keller K. Effect of fluid shear on mass transport in flowing blood. Fed Proc. 1971;30:1591–9.
22. Wang NHL, Keller KH. Solute transport induced by erythrocyte motions in shear flow. Trans Poly Alboc Artif Intern Organs. 1979;25:14–8.
23. Siedlecki CA, Lestini BJ, Kotte-Marchant K, Eppell SJ, Wilson DL, Marchant RE. Shear-dependent changes in the three-dimensional structure of human von Willebrand factor. Blood. 1996;88:2939–50.

J Biorheol (2009) 23:35–40
DOI 10.1007/s12573-009-0007-y

ORIGINAL ARTICLE

Deformability and adhesive force of artificial platelets measured by atomic force microscopy

Toru Wada · Yosuke Okamura · Shinji Takeoka · Ryo Sudo · Yasuo Ikeda · Kazuo Tanishita

Received: 10 January 2009 / Accepted: 30 April 2009 / Published online: 2 July 2009

Abstract Platelet glycoprotein GPIaIIa is an adhesive protein that recognizes collagen. We have investigated polymerized albumin particles conjugated with recombinant GPIaIIa (rGPIaIIa-poly Alb) for their platelet-like function. To evaluate the feasibility of these particles to achieve the hemostatic process, we measured the deformability (Young's modulus and spring constant) and the adhesive force of the particles using atomic force microscopy, which can measure the mechanical properties of individual cells. Our results showed that the Young's modulus of these particles was 2.3-fold larger than that of natural platelets and 12-fold larger than that of human red blood cells. The Young's modulus of the particles may have been determined by the properties of the polymerized albumin particle, although the glycoprotein of the platelet surface also contributed to the higher modulus. Our results also showed that the adhesive force of the rGPIaIIa-poly Alb with the collagen ligand was 52% of that of natural platelets. These two mechanical properties (deformability and adhesive force) of cells or particles, such as rGPIaIIa-poly Alb, are important specifications for the optimum design of platelet substitutes.

Keywords Adhesive force · Atomic force microscopy · Deformability · Glycoprotein GPIaIIa · Platelet substitutes · Thrombocytopenia · Young's modulus

T. Wada · K. Tanishita (✉)
Department of System Design Engineering,
Keio University, 3-14-1 Hiyoshi, Kohoku-ku,
Yokohama 223-8522, Japan
e-mail: tanishita@sd.keio.ac.jp

Y. Okamura · S. Takeoka
Department of Life Science and Medical Bioscience,
Waseda University, 3-4-1 Ohkubo,
Shinjuku-ku, Tokyo 169-8555, Japan

R. Sudo
Department of Biological Engineering,
Massachusetts Institute of Technology,
Cambridge, MA 02139-4307, USA

Y. Ikeda
School of Medicine, Keio University,
35 Shinanomachi, Shinjuku-ku, Tokyo 160-8582, Japan

Introduction

The total amount of platelets transfused annually worldwide has grown rapidly in recent years [1] primarily because platelet transfusion is the most effective therapy for bleeding associated with chemotherapy-induced thrombocytopenia or thrombocytopenia that develops following surgery. However, it is difficult to meet such a large demand for platelets due to their storage being limited to short-term periods and the risks involved in platelet transfusion, such as viral infections [2–4].

These difficulties can be overcome and the increased demand can be met by the use of platelet substitutes. The first of these was developed by Coller in 1980 [1] in the form of fibrinogen-coated beads that interacted with natural platelets, and numerous prototypes of platelet substitutes have been developed since [5, 6]. For example, Murata et al. [7] developed rGPIbα-liposomes, which are produced by incorporating a recombinant glycoprotein (GP)Ibα (an adhesive receptor on a platelet) to phospholipid bilayers of liposomes. Specific agglutination of rGPIbα-liposome to platelets occurs in the presence of von Willebrand factor (VWF) and ristocetin [8]. More recently, Takeoka et al. [9] developed polymerized albumin particles conjugated with recombinant glycoprotein Ibα (rGPIbα-poly Alb) and demonstrated (in in vitro experiments) the shear-

dependent adhesive property. In this type of platelet substitute, rGPIa/IIa-poly Alb, the glycoprotein GPIa/IIa is a receptor to the ligand of collagen and adheres to the collagen surface. The polymerized albumin particles represent a promising carrier for functional proteins because of their high blood compatibility and high biodegradability as well as the fact that they have been the subject of long-term study in clinical applications [10].

The major functions of platelets are adhesion and agglutination to the vascular injury region; consequently, the adhesive force is a major key to achieving such platelet functions. Therefore, any study that evaluates the feasibility of a platelet substitute to achieve the thrombogenic process must also determine the adhesive force of that platelet substitute. Atomic force microscopy (AFM) is the ideal method for measuring this adhesive force [11] because it can trace the surface topography of an individual living cell in a physiological medium and measure the adhesive force and elasticity of this cell by mapping the interactive forces.

A number of studies have demonstrated the effectiveness of using the AFM to measure the adhesive forces in cells. Lee et al. [12] directly measured the adhesive force of receptor-ligand and antibody–antigen associations in the immune system at a sensitivity of 10^{-14} N using AFM. Florin et al. [13] measured the adhesive force of the biotin–avidin association. (Biotin is a vitamin B complex and becomes inactivated by coupling with avidin specifically.) In their study, the Si_3N_4 tip of the AFM was first coated with bovine serum albumin (BSA), which adheres to biotin, and then the adhesive force was measured (160 ± 20 pN). Lee et al. [12] measured the adhesive force of streptavidin–biotin interactions under physiological conditions and identified the adhesive force to be due to individual streptavidin–biotin interactions. Holland et al. [14] measured the adhesive force of platelets adsorbed into a collagen substrate by using peptide-coated tips.

Another important mechanical property of platelets is deformability because it affects the lateral motion and aggregation process of platelets in the blood flow [15]. The deformability of platelets significantly affects the rolling and tethering of the platelets on the vascular surface. Therefore, a comprehensive evaluation of the feasibility of platelet substitutes involves the determination of both their adhesive force and deformability. Two measurable indicators of deformability are the spring constant and Young's modulus (elastic modulus). The deformability of red blood cells has been used as an important clinical diagnostic parameter; for example, Minamitani et al. [16] found that the Young's modulus of red blood cells from diabetic patients was higher than that from healthy patients.

In the study reported here, we have used AFM to measure the adhesive force, spring constant, and Young's modulus of platelet substitutes developed by Takeoka et al. [9], which are polymerized albumin particles conjugated with recombinant glycoprotein (rGPIa/IIa-poly Alb). For comparison, the same properties were measured for human red blood cells, poly Alb alone, and natural platelets, and for the respective aggregates of rGPIa/IIa-poly Alb, poly Alb, and natural platelets (activated by ADP for aggregation).

Materials and methods

Preparation of artificial platelets

In the platelet substitutes used here (rGPIa/IIa-poly Alb), the glycoprotein GPIa/IIa (Toray Industries, Toyko, Japan) is a receptor to the ligand of collagen and adheres to the collagen surface. The preparation of the polymerized albumin particles (poly Alb) has been described previously [9]. Here, the poly Alb was prepared in aqueous solutions to retain the hydrophilicity on the surface to ensure a high dispersing ability and a high capability for conjugation with water-soluble functional proteins. The size of rGPIa/IIa-poly Alb ranged from 1 to 2 μm. To monitor and therefore ensure the presence of rGPIa/IIa-poly Alb on the surface of the dish used in experiments, the particles were labeled with a fluorescein isothiocyanate (FITC) dye.

Preparation of red blood cells and natural platelets

Red blood cells (RBCs) were prepared as follows. Fresh human blood (9 ml) from healthy volunteers was added to a 0.29 *M* sodium citrate solution and then centrifuged at 156 *g* for 10 min. The resulting red cell pellets were rinsed with phosphate buffered saline (PBS) four times and then suspended in PBS to measure the deformability by AFM.

Natural platelets, as a platelet-rich plasma (PRP), were prepared as follows. Fresh human blood (9 ml) from healthy volunteers was added to a 0.013 *M* sodium citrate solution and centrifuged at 22,500 *g* for 15 s to separate PRP from the supernatant. The supernatant with free HEPES–Tyrode buffer was then centrifuged four times at 22,500 *g* for 15 s each time. The resulting supernatant with HEPES–Tyrode buffer was then mixed with 1.25 m*M* $CaCl_2$ and 6.25 mg/ml BSA and centrifuged at 352 *g* for 1 min. The final supernatant was PRP, which was then labeled with fluorescent probe carboxyfluorescein succinimidylester (CFSE) for visualization. Platelet aggregates were formed by adding ADP to the PRP, which activated the platelets.

Red cell ghosts were prepared from blood drawn from healthy volunteers into syringes containing a 0.29 *M* sodium citrate solution and then processed using the

hypotonic lysis method by Dodge et al. [17]. The resulting hematocrit was adjusted to 40% with PBS.

Immobilization of cells and particle samples

For immobilization, poly Alb, rGPIa/IIa-poly Alb, and PRP were individually mixed with PBS, placed on the surface of a sampling dish for 1 h at 4°C, and then rinsed four times with PBS. The FITC-labeled particles of poly Alb and rGPIaIIa-poly Alb were immobilized on the surface of the dish and confirmed by fluorescent microscopy.

Atomic force microscopy

The AFM system used to measure the adhesive force, spring constant, and Young's modulus of the immobilized cells and particles was a scanning probe microscope (NVB100; Olympus, Tokyo, Japan). The AFM probe was a cantilever (length 3 μm, curvature radius 15–20 nm) with a Si_3N_4 tip, and it had a spring constant of 0.09 N/m.

Measurement of deformability

The spring constant and Young's modulus were measured for natural platelets, rGPIa/IIa-poly Alb, poly Alb, RBC ghost, and RBCs. The spring constant was determined based on Hook's law, namely, by determining the gradient of the measured force curve. Figure 1 illustrates the contact process between the AFM cantilever and the sample surface. After the tip on the cantilever contacts with the sample surface, the cantilever starts to slightly deform upward, generating a compressive force on the sample and thus distorting the sample. The compressive force of the cantilever was measured as a function of this distortion of the sample. A plot of the compressive force versus distortion is referred to as the force curve (Fig. 1b). Assuming that the cell behaves as a spring, the spring constant K of the cell was calculated as

$$K = ky/(x - y) \tag{1}$$

where k is the spring constant of the cantilever, x is the displacement of the cantilever, and y is the deformation of the cantilever.

The Young's modulus of the cells or particles was determined based on the Hertz contact theory [18], which gives the mechanical relation between a sphere and a plane surface. Based on this Hertz contact theory, the tip surface was approximated as a sphere of curvature radius R; therefore, Young's modulus E of the cell was

$$E = \frac{3}{4}\frac{(1 - \nu^2) \times k}{R^{0.5}}\frac{y}{(x - y)^{1.5}} \tag{2}$$

where ν is the Poisson ratio of the cell or particle and was assumed to be 0.5. R is the radius of tip—20 nm in this case. Thus, E was determined by this expression based on the force curve.

Modification of the AFM probe

To measure the adhesive force of the cells and particles, the Si_3N_4 tip of the AFM must be coated with collagen type I (which is in subendothelial cells) in order to bind the GPIaIIa onto the surface of platelets. To coat the tip, the cantilever was incubated at 4°C for 24 h in a solution of 0.3 mg/ml collagen type I (pH 3) and then dried. The adhesive force was also measured using an uncoated probe to determine the adhesive force between Si_3N_4 and the sample cells or particles.

Measurement of adhesive force

The adhesive force of natural platelets, poly Alb, and rGPIaIIa-poly Alb was measured by drawing the cantilever away from the sample (Fig. 2a). Figure 2b illustrates the force curve used to determine the adhesive force. The adhesive force is the force generated by glycoprotein molecules (rGPIa/IIa) on the surface of poly Alb, which are activated by the collagen on the probe tip. The cantilever was deformed downward due to the adhesive force between the probe tip and the sample. The adhesive force F was determined by the deformation and spring constant k (= 0.09 N/m) of the cantilever as follows,

$$F = k\delta \tag{3}$$

Results and discussion

Figure 3 shows the measured spring constant and Young's modulus of natural platelets, rGPIa/IIa-poly Alb, poly Alb, RBC ghosts, and RBCs. The Young's modulus of RBCs was the lowest and is consistent with that of RBCs measured by Minamitani et al. [16]. The lower Young's modulus of RBCs has physiological implications; RBCs have a highly flexible structure that allow them to penetrate into narrow capillary vessels. Because the deformability of RBCs significantly affects the non-Newtonian nature of blood flow, many previous studies have focused on the influence of the deformability of RBCs on the lateral movement of cells [15]. However, a direct measurement of such deformability of RBCs is difficult due to the complicated shape of these cells. Many of the common measurement modalities used in earlier studies, such as micropipette aspiration, do not explicitly determine the elasticity of RBCs because of the complicated deformation

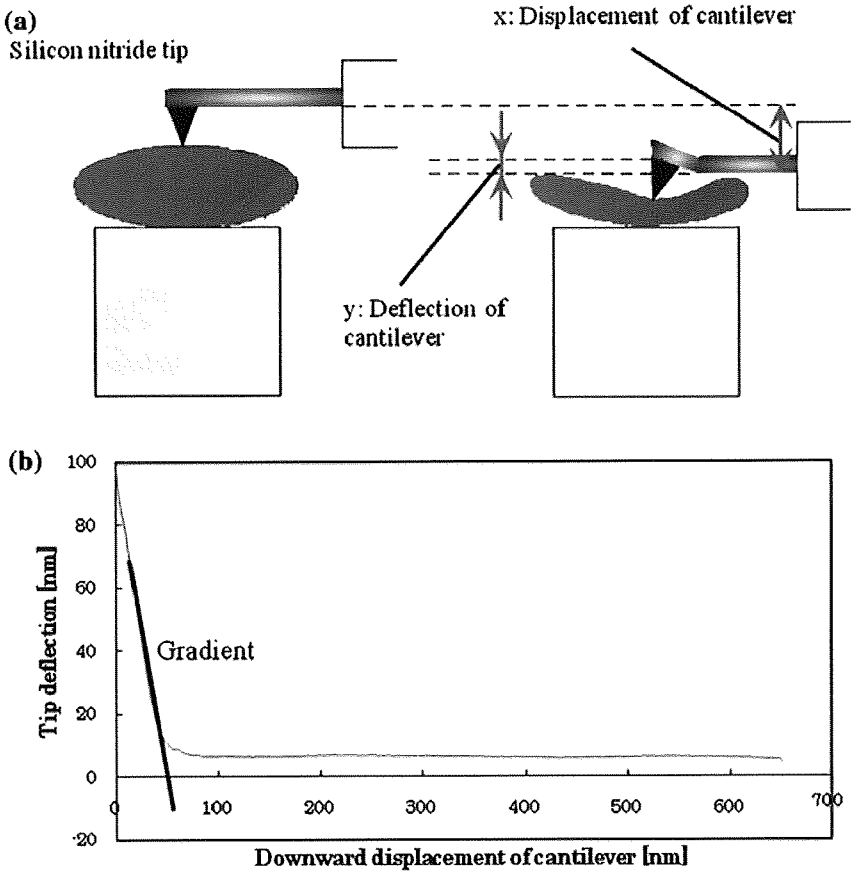

Fig. 1 **a** Schematic of cantilever displacement and deformation to measure the Young's modulus and spring constant of an individual cell or particle using an atomic force microscopy system. **b** The force curve

process [19]. In contrast, AFM provides a simple technique by which to determine the localized elasticity of an RBC membrane. The Young's modulus of the RBC ghosts was larger than that of the RBCs, possibly due to the processing of the RBC membrane during the preparation of the RBC ghosts. In comparison, the Young's modulus of the natural platelets was larger than that of the RBC ghosts, probably because a natural platelet is filled with intracellular structures, whereas RBCs and RBC ghosts consist of highly flexible membranes. The Young's modulus of poly Alb was larger than that of the natural platelets because poly Alb consists of packed polymerized albumin molecules, and the Young's modulus of rGPIa/IIa-poly Alb was slightly larger than that of poly Alb.

The Young's modulus was determined based on the force curve, which was not completely linear. In general, mechanical properties of RBCs are non-linear due to the viscoelastic properties of these cells, and Young's modulus of a cell or particle depends on deformation. In this study, therefore, the gradient of the force curve was determined from a linear portion of the force curve, namely, a small deformation range, which resulted in a Young's modulus of the natural platelets of 28 ± 9.8 kPa, compared with 5–50 kPa reported by Lee et al. [20].

Figure 4 shows the adhesive force measured using AFM. The adhesive force determined from the force curve reflects the interaction between the cell or particle and AFM tip surface. Thus, the tip surface significantly affects the interaction and, therefore, the adhesive force depends on the condition of the collagen coating. To confirm the effectiveness of collagen coating, we measured the adhesive force using a tip that was not coated with collagen. For all three samples (platelet, poly Alb with GPIa/IIa, and poly Alb without GPIa/IIa), the adhesive force measured with an uncoated tip was almost constant, indicating that the uncoated tip itself generated a slight interactive force of approximately 20 pN. To evaluate the actual adhesive force of the cell or particle, we subtracted this slight interactive force from the force measured with the coated tip for all three samples.

Figure 4 shows that the measured adhesive force of rGPIa/IIa-poly Alb was fourfold larger than that of poly Alb alone (without the glycoprotein rGPIa/IIa) and about half that of the natural platelets. Holland et al. [14] measured the adhesive force of natural platelets using AFM with a peptide-coated probe. The integrin receptor GPIIb/IIIa, which is a glycoprotein also found in the platelet, generated an interactive force with the probe. Holland et al.

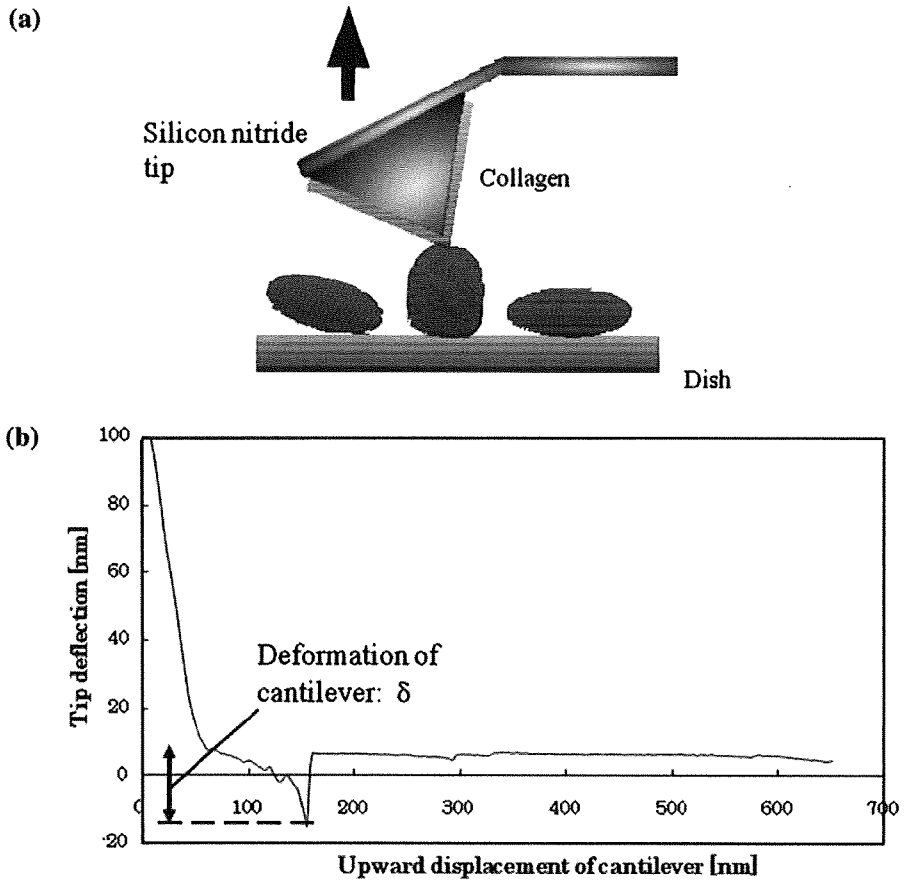

Fig. 2 **a** Schematic of cantilever displacement and deformation to measure the adhesive force between the receptor (glycoprotein rGPIa/IIa) and ligand (collagen) using an AFM system. **b** The force curve

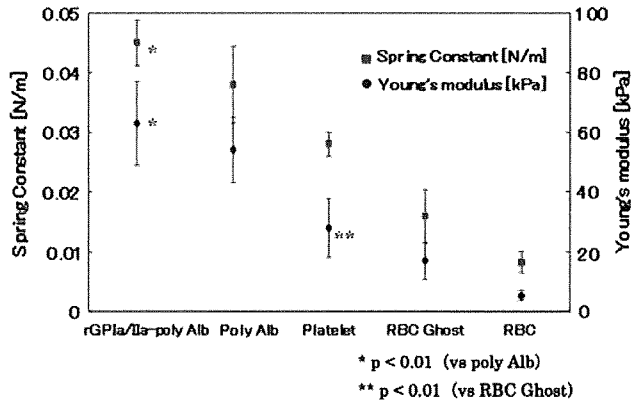

Fig. 3 Young's modulus and spring constant of an individual polymerized albumin particle (*poly Alb*) conjugated with the recombinant glycoprotein GPIaIIa (*GPIa/IIa-poly Alb*), poly Alb, natural platelet, red blood cell (*RBC*) ghost, and RBC, as measured using AFM. $*p < 0.01$ (vs. poly Alb), $**p < 0.01$ (vs. RBC ghost)

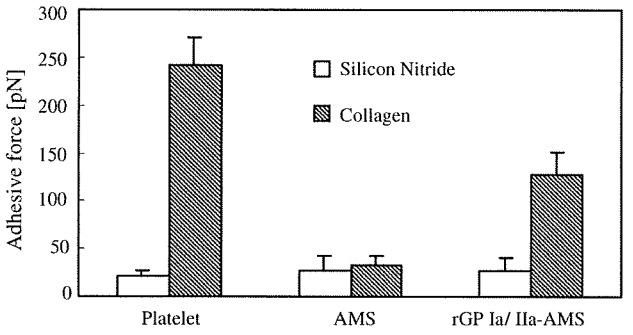

Fig. 4 Adhesive force of an individual natural platelet, poly Alb, and rGPIa/IIa-poly Alb, as measured by AFM

[14] also showed that a tip coated with an oligopeptide, GGGRGD, yielded an adhesive force of 660 pN and that a probe coated with GDGGAR, yet another oligopeptide, generated an adhesive force of 320 pN. In our study, the adhesive force of natural platelets was 242 ± 29 pN, which is close to that of the oligopeptide GDGGAR reported by Holland et al. [14], although the adhesive mechanism with peptides is different from that with collagen. In our study, the tip was coated with a collagen that is the ligand for a receptor of GPIa/IIa in the platelet. Because a platelet generates an adhesive force caused by the multi-site interaction with other receptors, such as GPIb

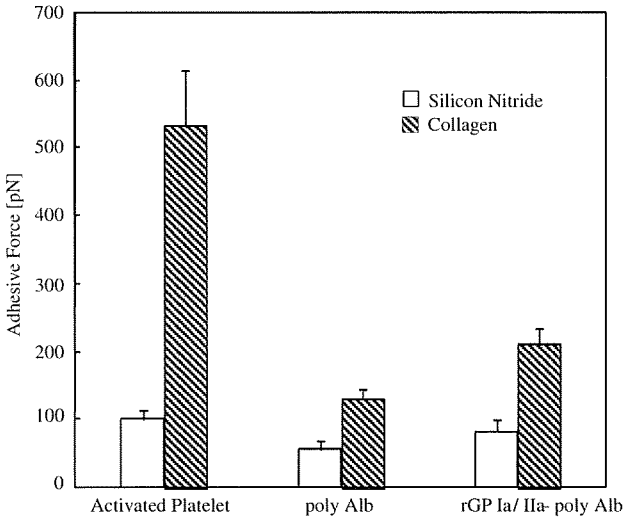

Fig. 5 Adhesive force of aggregates of natural platelets, poly Alb, and rGPIa/IIa-poly Alb, as measured by AFM

and GPIIb/IIIa, the adhesive force that we measured is only a part of the adhesive ability of natural platelets.

Figure 5 shows the measured adhesive force for the aggregates of cells and particles. All of the aggregates had an adhesive force larger than that of their respective single cell or particle because an adhesive force is generated between the AFM tip and aggregates. The adhesive force of the platelet aggregates was twice as large as that of a single platelet, and that of rGPIa/IIa-poly Alb was 64% larger than that of a single particle.

This study revealed that force mapping using AFM can quantify the adhesive force and deformability of an individual cell or particle. For artificial platelets, both of these properties are affected by the nature of the particle itself (e.g., albumin microspheres) and by the distribution of the receptor molecules (e.g., recombinant glycoprotein GPIaIIa) on the surface of the particle. These two mechanical properties are important specifications to be taken into account for the optimum design of artificial platelets, and their evaluation can be used to determine the feasibility of using artificial platelets.

Acknowledgment This work was supported by Health Science Research Grants (Artificial Platelets) from the Research on Advanced Medical Technology, Ministry of Health, Labour and Welfare, Japan.

References

1. Coller BS. Interaction of normal thrombasthetic and Bernard–Soulier platelets with immobilized fibrinogen: defective platelet–fibrinogen interaction in thrombasthenia. Blood. 1980;55:169–78.
2. George JN. Changes in platelet membrane glycoprotein during blood bank storage. Blood Cells. 1992;18:501–11.
3. Eaton LA, Read MS, Brinkhous KM. Glycoprotein Ib assays. Activity levels in Bernard–Soulier syndrome and in stored blood bank platelets. Arch Pathol Lab Med. 1991;115:488–93.
4. Kickler TS. Improving the quality of stored platelets. Transfusion. 1991;31:1–3.
5. Agam G, Livne A. Passive participation of fixed platelets in aggregation facilitated by covalently bound fibrinogen. Blood. 1983;61(1):186–91.
6. Agam G, Livne A. Erythrocytes with covalently bound fibrinogen as a cellular replacement for the treatment of thrombocytopenia. Eur J Clin Invest. 1992;22(2):105–12.
7. Murata M, Ware J, Ruggeri ZM. Site-directed mutagenesis of a soluble fragment of platelet glycoprotein Ibα demonstrating negatively charged residues involved in von Willebrand factor binding. J Biol Chem. 1991;266:15474–80.
8. Kitaguchi T, Murata M, Iijima K, Kamide K, Imagawa T, Ikeda Y. Characterization of liposomes carrying von Willebrand factor-binding domain of platelet glycoprotein Ibalpha: a potential substitute for platelet transfusion. Biochem Biophys Res Commun. 1999;261(3):784–9.
9. Takeoka S, Teramura Y, Ohkawa H, Ikeda Y, Tsuchida E. Conjugation of von Willebrand factor-binding domain of platelet glycoprotein Ibα to size-controlled albumin microspheres. Biomacromolecules. 2000;1(2):290–5.
10. Gupta PK, Hung CT. Albumin microsphere I: physicochemical characteristics. J Microencapsul. 1989;6:262–427.
11. Jena BP, Hörber JKH. Atomic force microscopy in cell biology. San Diego: Academic Press; 2002. p. 67.
12. Lee GU, Kidwell DA, Colton RJ. Sensing discrete streptavidin–biotin interactions with atomic force microscopy. Langmuir. 1994;10:354–7.
13. Florin EL, Moy VT, Gaub E. Adhesion forces between individual ligand-receptor pairs. Science. 1994;264:415–7.
14. Holland NB, Siedlecki CA, Marchant RE. Intermolecular force mapping of platelet surfaces on collagen substrata. J Biomed Mater Res. 1999;45:167–74.
15. Goldsmith HL, Marlow JC. Flow behavior of erythrocytes. J Colloid Interface Sci. 1979;71(2):383–407.
16. Minamitani H, Kawamura T, Tsukada T, Iijima A, Sekizuka E, Osho C. Measurement of elasticity of erythrocytes using atomic force microscope. Trans IEE Jpn. 2002;122:1664–71.
17. Dodge JT, Mitchell C, Hanahan DJ. The preparation and chemical characteristics of hemoglobin-free ghosts of human erythrocytes. Arch Biochem Biophys. 1962;100:119.
18. Hertz H. Über die Berühung fester elastischer Körper. J Reine Angew Math. 1882;92:156–71.
19. Evans EA, Skalak R. Mechanics and thermodynamics of biomembranes, CRC critical reviews in Bioengineering. vol. 3, issues 3 & 4. Boca Raton: CRC Press; 1979.
20. Lee IS, Marchant RE. Force measurements on platelet surfaces with high spatial resolution under physiological conditions. Colloids Surf B Biointerfaces. 2000;19:357–65.

ADVANCED FUNCTIONAL MATERIALS www.afm-journal.de

Adhesive, Flexible, and Robust Polysaccharide Nanosheets Integrated for Tissue-Defect Repair

By *Toshinori Fujie, Noriyuki Matsutani, Manabu Kinoshita, Yosuke Okamura, Akihiro Saito,* and *Shinji Takeoka**

Recent developments in nanotechnology have led to a method for producing free-standing polymer nanosheets as a macromolecular organization. Compared with bulk films, the large aspect ratio of such nanosheets leads to unique physical properties, such as transparency, noncovalent adhesion, and high flexibility. Here, a biomedical application of polymer nanosheets consisting of biocompatible and biodegradable polysaccharides is reported. Micro-scratch and bulge tests indicate that the nanosheets with a thickness of tens of nanometers have sufficient physical adhesiveness and mechanical strength for clinical use. A nanosheet of 75 nm thickness, a critical load of 9.1×10^4 N m^{-1}, and an elastic modulus of 9.6 GPa is used for the minimally invasive repair of a visceral pleural defect in beagle dogs without any pleural adhesion caused by wound repair. For the first time, clinical benefits of sheet-type nano-biomaterials based on molecular organization are demonstrated, suggesting that novel therapeutic tools for overlapping tissue wounds will be possible without the need for conventional surgical interventions.

1. Introduction

Recent developments in nanotechnology have led us to the fabrication of quasi two-dimensional free-standing ultrathin polymer films called polymer nanosheets.[1–5] Work in this area has focused on their macromolecular organization to exploit their unique properties, such as high flexibility, adhesiveness, and transparency. These attractive properties are derived from the large aspect ratio of the size of the film (over 10^6); they are approximately 1 cm laterally and tens of nanometers thick, giving them similar dimension to a cell membrane or the extracellular matrices in living organisms. Quite recently, a free-standing polymer nanosheet composed of biodegradable and biocompatible polysaccharides (i.e., a polysaccharide nanosheet) was fabricated in our laboratory.[6,7] The polysaccharide nanosheet was fabricated through a spin-coating assisted layer-by-layer (LbL) method,[8–11] using alternating deposition of oppositely charged polyelectrolytes via electrostatic interactions, a novel method for macromolecular organization that does not require any chemical cross-linkers. Subsequently, we demonstrated the straightforward transference of the polysaccharide nanosheet onto human skin[6] or its surface modification with nano- or micrometer-sized particles,[7] while keeping a high aspect ratio using a water-soluble sacrificial membrane. In our previous study, we found that the flexible polysaccharide nanosheets densely overlap and adhere to the skin surface or micrometersized objects through physical adsorption, such as van der Waals interactions, and works like an adhesive plaster for a wound dressing.

We have developed the concept of such a "nano-adhesive plaster" for wound repair in surgery. Surgical repair of tissue defects is basically achieved by three fundamental maneuvers: suture, plication, and overlapping. Despite their high reliabilities for wound repair, the conventional repair of a pleural defect by suture and plication usually reduces the volume of pulmonary tissue, thereby decreasing respiratory functions. Pulmonary air leakage due to visceral pleural injury is one of the most common postoperative complications after thoracic surgery. It might be caused by the prolonged placement of a drainage tube and/or longer hospitalization, and worst of all, it may lead to thoracic empyema. Therefore, the tight and firm repair of a pleural injury/defect is really important to prevent air leakage.[12,13] Nevertheless, it is sometimes difficult to practically suture or plicate a large defect or fragile tissue of the emphysematous lung. Overlapping is therefore considered to be an ideal maneuver to repair a pleural defect because it simply seals the injured surface without reducing the tissue volume of the injured lung. Some investigators

[*] Prof. S. Takeoka, Dr. T. Fujie, Dr. Y. Okamura
Department of Life Science and Medical Bioscience
Faculty of Science and Engineering, Waseda University, TWIns
2-2 Wakamtsu-cho, Shinjuku-ku, Tokyo 162-8480 (Japan)
E-mail: takeoka@waseda.jp
Prof. S. Takeoka
Consolidated Research Institute for Advanced Science and Medical Care, Waseda University
513, Wasedatsurumaki-cho, Shinjuku-ku, Tokyo 162-0041 (Japan)
Dr. N. Matsutani
Department of Surgery, National Defense Medical College
Tokorozawa, Saitama 359-8513 (Japan)
Dr. M. Kinoshita
Department of Immunology and Microbiology, National Defense Medical College
Tokorozawa, Saitama 359-8513 (Japan)
A. Saito
Department of Life Science and Medical Bioscience
Graduate School of Advanced Science and Engineering
Waseda University, TWIns
2-2 Wakamtsu-cho, Shinjuku-ku, Tokyo 162-8480 (Japan)

DOI: 10.1002/adfm.200900103

have demonstrated the efficacy of fibrin glue (sheet) composed of fibrin-glue-coated collagen fleece, a typical adhesive material, for the repair of a visceral pleural defect.[14] However, this material will cause severe pleural adhesion. In the case of high-risk patients with respiratory failure, such a severe pleural adhesion might further deteriorate pulmonary dysfunctions, a serious complication for the compromised patients. Therefore, a novel tissue sealant that does not cause tissue adhesion is required.

Here, we report the potential biomedical application of adhesive, flexible, and robust polymer nanosheets in a surgical intervention. More concretely, we report the development of a versatile method of fabricating biocompatible polysaccharide nanosheets including evaluation of their physiological, adhesive, and mechanical properties, as well as investigation of the working mechanism of the polysaccharide nanosheet at the nano/bio interface between the nanosheet and reconstructing tissues in wound repair. Such a film was used in a practical working test to repair a visceral pleural defect in a minimally invasive way without any pleural adhesion.

2. Fabrication of Free-Standing Polysaccharide Nanosheets

A polysaccharide nanosheet was fabricated on a SiO_2 substrate by a spin-coating-assisted layer-by-layer (SA-LbL) method,[15,16] using chitosan and sodium alginate (Na alginate) polyelectrolyte solutions. Chitosan and Na alginate were chosen for the components of the polymer nanosheet because of their biocompatibility and biodegradability. Na alginate is a water-soluble polymer, and chitosan is an enzymatically degradable polymer; both are typical components of wound-dressing materials.[17–19] However, polysaccharides are generally brittle because of high crystallinity introduced by inter- and intramolecular secondary bonding.[19–21] We focused on the SA-LbL approach because this method produced a versatile ultrathin film with a flat and smooth surface by multilayering the polysaccharides in close to single molecular layers free from deformation. We confirmed the multilayer structure of chitosan and Na alginate by ellipsometric and IR spectroscopic analysis, which showed the thickness of one layer pair, calculated to be approximately 2.9 nm, consisted of electrostatic interactions. Previously, we demonstrated a sacrificial layer method in order to obtain a free-standing polysaccharide nanosheet, which is applicable to a maximum sheet size of 9 cm^2 with a thickness of tens of nanometers.

In order to obtain a large nanosheet, we chose to adopt the "supporting film" method reported by Whitesides and co-workers.[22] This method allows the convenient collection of free-standing nanosheets by peeling a dried bilayered film from a SiO_2 substrate. The bilayered film consists of the polymer nanosheets supported by a water-soluble thin film such that the interaction between the bilayered components is higher than that between the polymer nanosheet and SiO_2 substrate, thereby facilitating the removal of the film. Following the method shown in Figure 1a, a 10 wt% concentrated poly(vinyl alcohol) (PVA) aqueous solution was cast on a polysaccharide-covered substrate and dried for 12 h until a robust PVA film was obtained. The resulting bilayered film composed of the polysaccharide nanosheet with a thickness of several tens of nanometers and the ~70 μm thick PVA film was easily peeled from the edge of the SiO_2 substrate with tweezers, and the nanosheet can be released into an aqueous solution by dissolution of the PVA film. The polysaccharide nanosheet can thus be transferred onto the tissue-defect site by simply adding water to the bilayered film (Fig. 1b). This water-mediated release methodology is suitable for wound dressing because the procedure does not require any organic solvents.

The overall shape of the bilayered film corresponded to that of the substrate (Fig. 2a). As the bilayered film was gently immersed into a petri dish filled with a phosphate buffer saline (PBS: pH 7.4, 37 °C) solution, the water-soluble PVA layer was immediately dissolved to obtain an ultrathin film in a free-standing state that was approximately 4 cm in diameter, corresponding in size and shape to those of the original SiO_2 substrate (Fig. 2b). The resulting free-standing nanosheet was transparent, very flexible, and not swelled in an aqueous condition; it could be flapped by manipulating with tweezers. Moreover, it is the largest noncovalently bonded free-standing polymer nanosheet to date, as far as we know. We next microscopically observed the surface morphology of the polysaccharide nanosheet consisting of

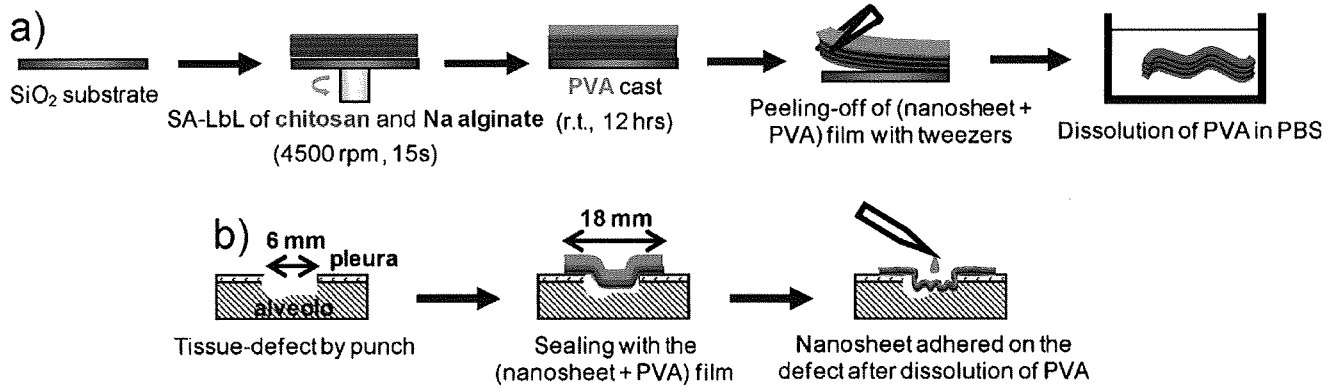

Figure 1. Schematic representation of the polysaccharide nanosheet integrated for tissue-defect repair. a) Fabrication method for a free-standing polysaccharide nanosheet using an SA-LbL method and a water-soluble supporting PVA film. b) Schematic explanation of tissue-defect repair using a polysaccharide nanosheet.

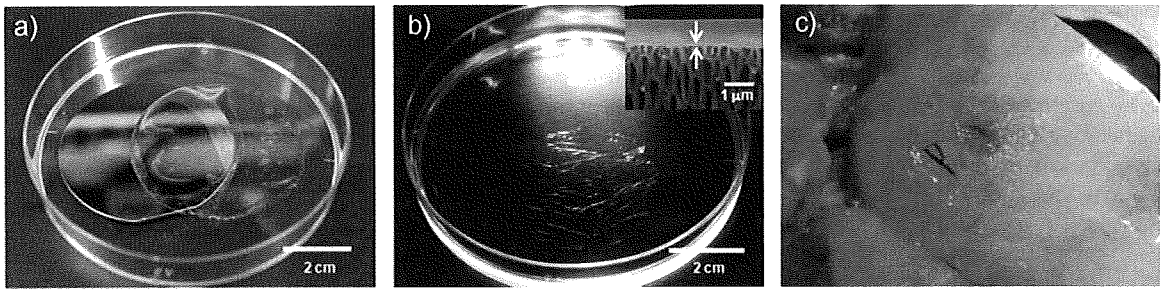

Figure 2. Tissue defect repaired by a polysaccharide nanosheet using a water-soluble supporting membrane. a) A bilayered film, consisting of a 75 nm polysaccharide LbL ultrathin film and a 70 μm water-soluble PVA supporting film, peeled from a SiO_2 substrate. b) A free-standing 75 nm polysaccharide nanosheet floating in PBS approximately 4 cm in diameter, retaining the shape of the SiO_2 substrate. The inset shows an scanning electron microscopy (SEM) cross-sectional view of the 75 nm polysaccharide nanosheet on an alumina porous membrane (the white arrows indicate the location of the polysaccharide nanosheet). c) A polysaccharide nanosheet supported by a PVA membrane sealing the visceral pleural defect of a beagle dog. The capital P was marked on the surface of the PVA membrane in order to distinguish the bilateral side.

20.5 layer pairs of polysaccharides deposited on a porous alumina membrane (Anodisc) using scanning electron microscopy (SEM) and found a smooth and flat surface sheet that was 75 nm thick (Fig. 2b, inset).

The specific thickness of the nanosheet was measured using a probe-type scanning surface profiler on the SiO_2 substrate after three exchanges of PBS, resulting in a value of 35 ± 2.3 nm when we used 10.5 layer pairs of polysaccharides in the preparation, and corresponding to the thickness before PVA casting (i.e., 35 ± 2.1 nm, measured by the surface profiler). The root-mean-square (RMS) surface roughness was quite low (2.4 ± 0.52 nm). A single layer pair of the nanosheet was calculated to be approximately 3.3 nm by dividing the thickness with the number of layer pairs.[15] This value indicates that, each polysaccharide was assembled inside the nanosheet in almost a single molecular layer. Following this result, we prepared several polysaccharide nanosheets of varying thickness; this was accomplished by controlling the number of layers during the SA-LbL process, the thickness being proportional to the number of layer pairs (Fig. S1, Supporting Information). Although the typical cast polysaccharide film that was over 1 μm in thickness tended to be brittle, the free-standing polysaccharide nanosheets were highly flexible. This is due to the appearance of a "liquid-like" layer inside the nanosheet, resulting from the relaxation of the individual polymer chains on decreasing the thickness of the film.[23] Moreover, a polysaccharide nanosheet mounted on a wire loop was very stable for at least three months in dry conditions, and was quite stable with respect to maintaining its shape for over three months in water. Moreover, the half-life of the thickness of a 75 nm thick polysaccharide nanosheet was 11 days in a physiological condition (pH 7.4 in PBS, 37 °C). Therefore, we succeeded in the versatile fabrication of a free-standing polysaccharide nanosheet using a water-soluble supporting film.

3. Physiological Properties of Polysaccharide Nanosheets

A polysaccharide nanosheet in the form of a bilayered film can be transferred onto the visceral pleural defect site of a beagle dog by dissolution of the PVA film (Fig. 2c). In the practical biomedical application of polysaccharide nanosheets, bleeding from the defect site is a general risk of a surgical operation. However, because of the robust and flexible properties of the nanosheets, this polysaccharide nanosheet not only inhibited the permeation of blood components from the defect site, but also determined the position of blood clots accumulated along the interface of the nanosheet, which should induce and stimulate the subsequent growth position of the fibroblast cells and angiogenesis in the tissue-defect sites. To test whether this was so, we dropped human

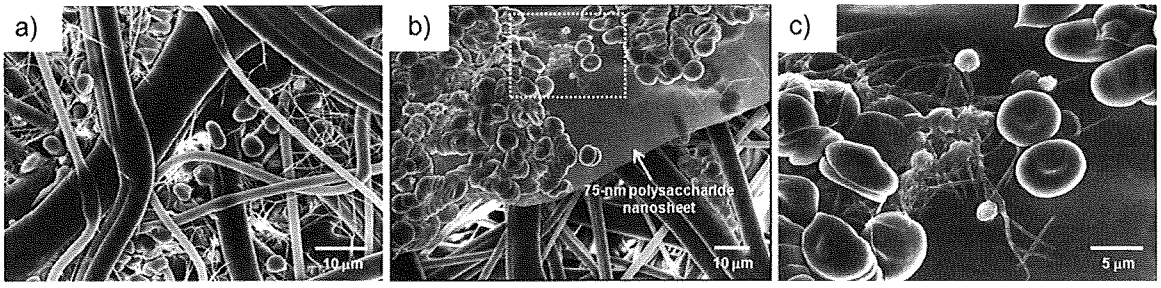

Figure 3. Physiological effect of the polysaccharide nanosheet contacting blood cells. a) SEM image of blood cells flowing into a PP fibrous mesh. b) SEM image of blood cells deposited on the surface of a 75 nm polysaccharide nanosheet overlapping the PP fibrous mesh. c) Magnified SEM image of the dashed square region in b. The physiological morphology of activated platelets was observed with spreading pseudopodia where the polysaccharide nanosheet was acting as a scaffold for platelet adhesion.

blood onto a polysaccharide nanosheet prepared on a poly(propylene) mesh filter. Although blood cells, mainly erythrocytes, easily permeated into the fibrous mesh (Fig. 3a), they stagnated on the surface of the polysaccharide nanosheet without distortion and penetration into the nanosheet and without hemolysis of blood cells (Fig. 3b). Additionally, we observed that some platelets were partially adhered on the surface of the nanosheet with spreading pseudopodia (Fig. 3c). This polysaccharide nanosheet may act not only as a barrier, but also as a scaffold for in-flow blood cells in a process of hemostasis. It is noteworthy that the polysaccharide nanosheet provides the hetero-interface for the tissue-defect sites whether they are to be repaired or not by working as a separator against incoming blood flow, where the subsequent growing position of fibroblast cells will be clearly determined by the position of formulated blood clots. Moreover, considering that the primary mechanical strength of the tissue-defect sites repaired by the nanosheet may be fragile, the formation of normal blood clots will reinforce the nanosheet strength.

Additionally, a Lee–White test[24,25] was undertaken to judge the blood pro-coagulation property of the polysaccharide nanosheet by observing the substrate surface (see Supporting Information). We overlaid a polysaccharide nanosheet on the surface of a polypropylene (PP) substrate where whole blood showed poor coagulation. After incubation in whole human blood for 30 min and gentle rinsing with PBS, some blood clots were observed at the interface of the substrate covered with the polysaccharide nanosheet, while few clots were observed at the native PP surface (Fig. S2, Supporting Information). Interestingly, we did not obtain strong blood pro-coagulation activity as reported by Akashi and co-workers,[24] who used dipped chitosan LbL films. The difference could be attributed to differences in the surface roughness; spin-coating leads to low RMS roughness while dipping results in high RMS roughness in the LbL system.[26] Using a technique that results in a very weak pro-coagulant activity and that does not require an anti-coagulant agent (e.g., heparin) is a clinical advantage because postoperative embolism is due to the strong pro-coagulant activity[27] and/or the heparin-induced thrombocytopenia (HIT).[28] Therefore, one of the major problems in clinical situations can be avoided by using the polysaccharide nanosheet.

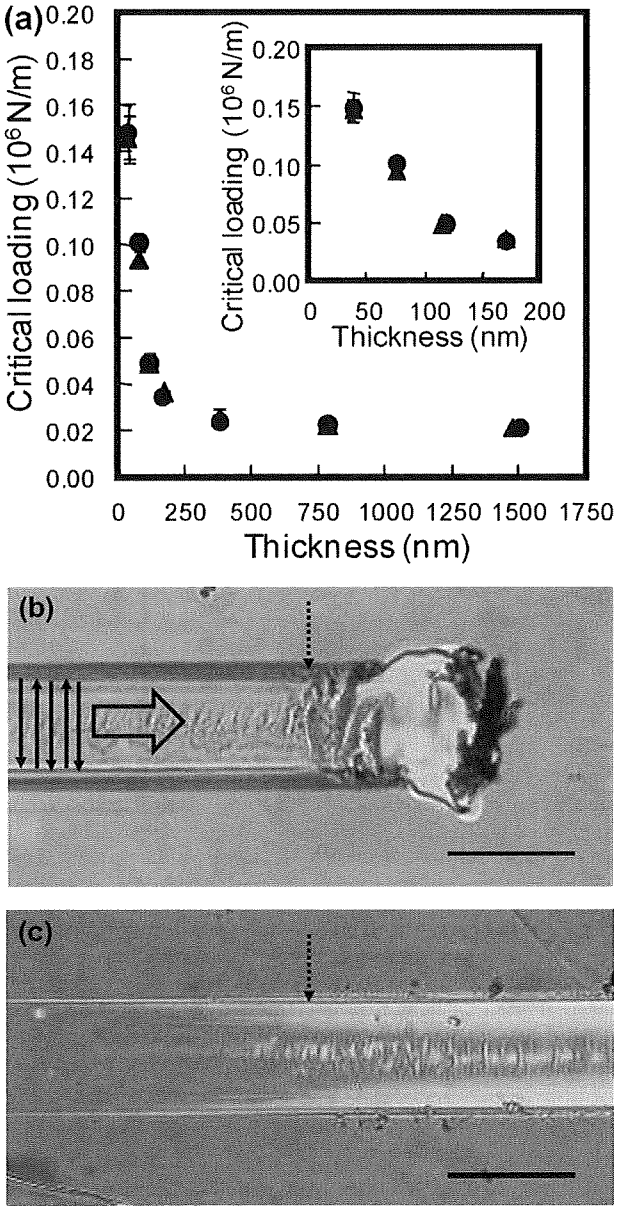

Figure 4. Evaluation of adhesive properties of the polysaccharide nanosheets. a) The relationship between the critical load and the thickness of the polysaccharide nanosheet before (circle) and after (triangle) detachment of the nanosheet. Inset: expansion of the graph for thickness <200 nm. b,c) Microscopic observations after micro-scratch test of the polysaccharide nanosheets with a thickness of 1482 (b) and 77 nm (c). Black arrows show the direction of the stylus on the nanosheet, and dashed arrows indicate detached points from the SiO_2 substrate. Scale bars show 100 μm.

4. Adhesive and Mechanical Properties of Polysaccharide Nanosheets

In order to determine the optimum thickness of the polysaccharide nanosheet for in vivo tissue-defect repair usage, the micro-scratch and bulge tests were performed. We utilize the micro-scratch test[29] for the evaluation of macroscopic adhesive properties of ultrathin films, such as nanosheets. The micro-scratch tester employs a diamond stylus, which oscillates parallel to the surface of the polysaccharide nanosheet on the SiO_2 substrate. The adhesive failure of the nanosheet with the stylus was detected as "critical load" of the polysaccharide nanosheet, which is a relative value of the adhesive force. Adhesive properties of the polysaccharide nanosheets did not change before and after detachment. Interestingly, the critical load of the polysaccharide nanosheets was drastically increased as the thickness was decreased below 200 nm; the critical load of a thickness of 39 nm was approximately 7.5 times that of a 1482 nm nanosheet (Fig. 4a). Moreover, microscopic observation revealed different trails after scratching nanosheets with a thickness above and below 200 nm; i.e., "cut-off" trails at 1482 nm and "drawn" trails at 77 nm (Fig. 4b, c and S3, Supporting Information. This suggested that the elasticity of thin films would be different for thicknesses above and below 200 nm. Therefore, we selected the top three adhesive nanosheets for the evaluation of mechanical properties.

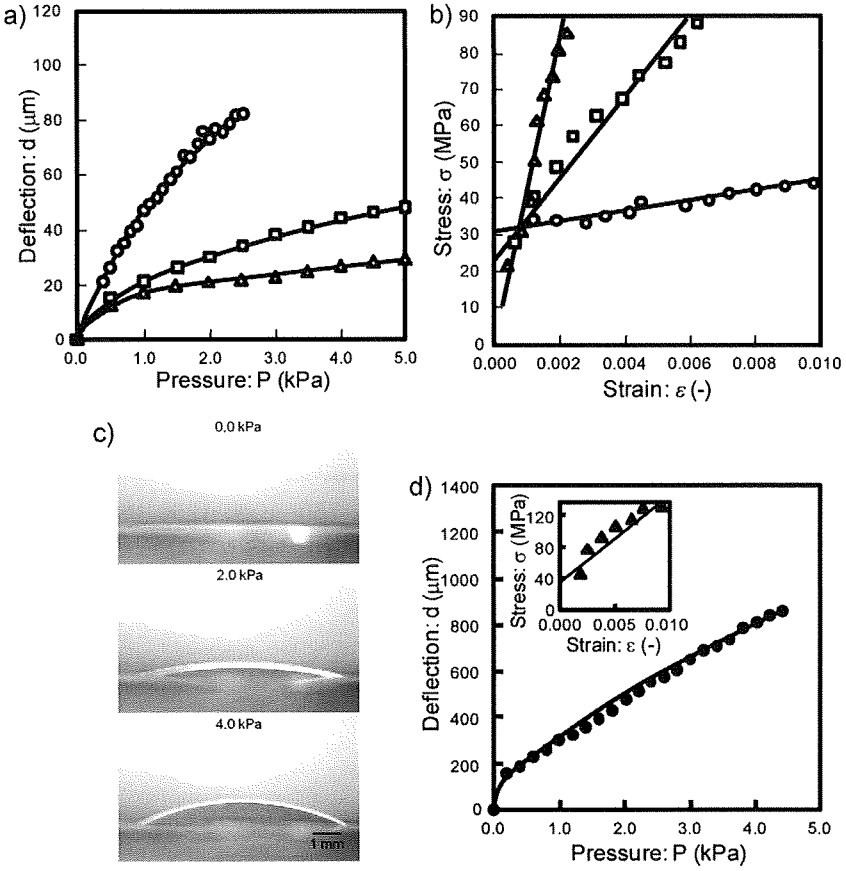

Figure 5. Evaluation of mechanical properties of the polysaccharide nanosheets. a) Pressure–deflection and b) stress–strain curves using a 1 mm diameter circular hole for various thicknesses of polysaccharide nanosheets (open circle: 35 nm, open square: 75 nm, open triangle: 114 nm). c) Sequential macroscopic cross-sectional views of the deflected 75 nm polysaccharide nanosheet when different pressures were applied through the 6 mm diameter hole. d) The corresponding pressure–deflection curve (inset: stress–strain curve).

The bulge test has been frequently used for the evaluation of the mechanical strength of ultrathin films.[30–32] Following the microscratch test, we prepared three types of polysaccharide nanosheets with different thicknesses (35, 75, and 114 nm), which were transferred onto steel plates with either a 1 or 6 mm diameter circular hole in the center (Fig. S4). It is noteworthy that the polysaccharide nanosheet easily adhered to the steel plate without using chemical adhesion. The nanosheet on the steel plate was then placed in a custom-made steel chamber. As pressure was applied to the polysaccharide nanosheet through the circular hole of the plate, a deflection of the nanosheet was monitored from a side-view of the plates until distortion occurred. During the bulge test, the monitoring environment was kept at ambient conditions (temperature: 25 ± 1 °C, humidity: 37 ± 3%) because the molecular dynamics of polyelectrolytes are influenced by temperature and humidity; high humidity over 70% in the bulge test showed irregular expansion of the polysaccharide nanosheet due to incorporation of water molecules, resulting in the false evaluation of the potential elastic modulus of the nanosheet. The typical elastic behavior of the 35 nm polysaccharide nanosheet on a 1 mm diameter hole was recorded in Movie S1 (Supporting Information). The relationship between pressure and deflection was nonlinear, and the overall deflection of the polysaccharide nanosheet was damped by an increment of the thickness. This suggested the elasticity of the polysaccharide nanosheet was dependent on the total film thickness (Fig. 5a). We then converted the values derived from the pressure–deflection curve into a stress–strain curve. From the initial elasticity of the stress–strain curve (Fig. 5b), the ultimate tensile strength (σ_{max}), elongation (ε_{max}), and elastic modulus (E) were calculated for different thicknesses (Table 1).

Table 1. Mechanical properties of the polysaccharide nanosheets.

Hole diameter (a) [mm]	Thickness (h) [nm]	Ultimate tensile strength (σ_{max}) [MPa]	Ultimate tensile elongation (ε_{max}) [%]	Elastic modulus (E) [GPa]
1	35 ± 2.1	51 ± 5	3.2 ± 0.1	1.1 ± 0.4
1	75 ± 4.1	123 ± 8	6.0 ± 3.0	8.1 ± 2.5
1	114 ± 5.8	116 ± 20	3.6 ± 1.4	11.0 ± 1.6
6	75 ± 4.1	159 ± 30	6.5 ± 5.6	9.6 ± 3.1

The elastic modulus of the 35 nm polysaccharide nanosheet was 1.1 ± 0.4 GPa, which is a similar value to that ($E = 1.5$ GPa) of the polymer nanosheet composed of poly(allylamine hydrochloride) and poly(sodium styrenesulfonate) with the same thickness (35 nm) reported by Tsukruk and co-workers;[1] it is considerably smaller than the typical elastic modulus of a cellulose film ($E = 15$ GPa) fabricated from the similarly structured molecule chitosan with a thickness of over 1 μm. This result suggested that polymer nanosheets with a thickness of tens of nanometers were quite flexible due to the low elastic modulus. As the thickness of the polysaccharide nanosheet was increased, the ultimate tensile strength and the elastic modulus recorded similar values (75 nm: $\sigma_{max} = 123 \pm 8$ MPa, $E = 8.1 \pm 2.5$ GPa; 114 nm: $\sigma_{max} = 116 \pm 20$ MPa, $E = 11.0 \pm 1.6$ GPa). These results are in good agreement with the report by Rubner and co-workers[33] where the elastic modulus of ultrathin films composed of poly(allylamine hydrochloride) and poly(sodium styrenesulfonate) reached a plateau value when the thickness was close to 70 nm. Generally, ultrathin polymer films with thickness of tens of nanometers show glass-transition temperatures lower than the corresponding bulk.[32] This reflects a specific interfacial property of the ultrathin film, such as unrestricted macromolecular mobility, and is probably the reason why such nanosheets have low elastic moduli. In support of this assumption, some of the 114 nm polysaccharide nanosheets spontaneously detached from the steel plate as the thickness of the nanosheet was increased before breaking by the bulge test (data not shown);this strongly suggested that thickness, flexibility in sheets with a thickness on

the order of tens of nanometers, and low elastic modulus have a good relationship with the physical adhesive properties of the nanosheet, as shown in Figure 4a. It is noteworthy that Tsukruk and co-workers[34] reported free-standing silk fibroin nanosheets (<100 nm thick), which showed the ultimate tensile strength of 100 MPa and an elastic modulus of 6–8 GPa. This suggests that the 75 nm polysaccharide nanosheets should possess a robust structure with the ultimate tensile strength of 123 MPa and an elastic modulus of 8 GPa, similar to that of the silk fibroin nanosheets. Therefore, we performed a bulge test using a 75 nm polysaccahride nanosheet overlapping a 6 mm diameter hole because it was expected to have a higher capacity in adhesiveness and robustness than the 114 nm and 35 nm nanosheets, respectively. The elastic modulus of this nanosheet, 9.6 ± 3.1 GPa (σ_{max}: 159 MPa, ε_{max}: 6.5%), was similar to that of the same film on the 1 mm diameter hole. The standard deviation (SD) value of the 6 mm modulus was slightly larger than that of 1 mm due to the difficulty of maintaining a homogenous in-flow pressure to the nanosheet for the large hole. Furthermore, no distortion of the 75 nm nanosheet was found until a pressure of 4.5 kPa was reached (Fig. 5c and d). This is an important result because a pressure of 30 cm H_2O (approximately 3 kPa) is a clinically important criteria in tissue-defect repair applications. This pressure is a physiologically expected typical value in normal respiration with the lungs, and has been noted in connection with wound dressings such as fibrin sheets.[35–37] Hence, as the 75 nm nanosheet was stable to pressures well over this value, we decided that the 75 nm thickness was appropriate for a clinical application using beagle dogs.

5. Repairing a Pleural Defect With a Polysaccharide Nanosheet

We demonstrated a practical working test of the 75 nm polysaccharide nanosheet for an in vivo visceral pleural defect model of beagle dogs. Overlapping pleural defect by a fibrin sheet is clinically one of the most conventional therapies for pleural repair. The polysaccharide nanosheet, or a fibrin sheet used as a positive control, was placed onto a pleural-defect area prepared by a 3.2 cm^2 aorta punch on the right anterior, middle, and posterior lobes (Movie S2 and S3, Supporting Information). The 75 nm polysaccharide nanosheet was placed on a supporting PVA film (70 μm in thickness) for handling. Then the PVA film was dissolved with PBS solution as shown in Figure 1b, until the letter "P" marked on the surface of the PVA (visible in the optical microscopic image in Fig. 2c) was removed. As the PVA film was dissolved, the underlying polysaccharide nanosheet fitted onto the curvature of the remaining tissue fully overlapping the pleural defect without any chemical adhesive. After drying for a few minutes, the polysaccharide nanosheet completely assimilated to the tissue surface. The pressure resistance of the repaired site was determined at 5 min, 3 h, and 24 h after repair. The airway pressure at which air leakage occurred (termed "bursting pressure") was measured using a manometer and was individually measured for each repaired lobe, while the bronchi of the other two lobes were clamped. The highest airway pressure applied was 60 cm H_2O because air leakage could occur from the intact pulmonary hilum at pressures above 60 cm H_2O. At 5 min after repair, the polysaccharide nanosheet showed a lower bursting pressure

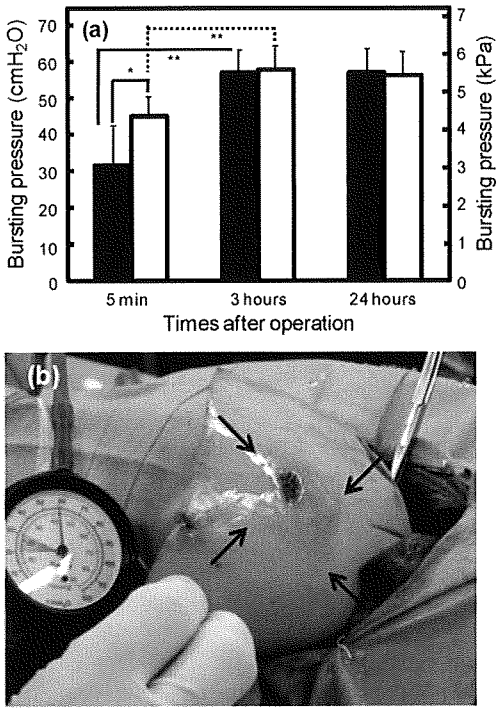

Figure 6. Visceral pleural defect repair using a polysaccharide nanosheet. a) Time-course changes in bursting pressure (in cm H_2O, left, and kPa, right) after repair using the polysaccharide nanosheet (black bars) or fibrin sheet (white bars). The difference in the bursting pressures of the polysaccharide nanosheet and fibrin sheet is indicated by * ($p < 0.05$); the difference in those measured 5 min and 3 h after repair are indicated by ** ($p < 0.05$). b) Polysaccharide nanosheet with a thickness of 75 nm secured the repaired defect when pressurized by over 50 cm H_2O pressure at 3 h after repair. The region indicated by arrows shows the nanosheet-sealed area.

(31.7 ± 10.3 cm H_2O) than that of the fibrin sheet (45.0 ± 5.5 cm H_2O) (Fig. 6a). The bursting pressure of the polysaccharide nanosheet was slightly lower than that found in the bulge test (~45 cm H_2O for 6 mm diameter hole prepared on the steel substrate). The reason for this discrepancy in the nanosheet bursting pressure might be due to the repeated stretch and/or expansion of the pulmonary surface by ventilation. At 3 h after repair, the outline of the square polysaccharide nanosheet assimilating to the tissue surface could be faintly seen (Fig. 6b, indicated by arrows), and the mechanical durability was dramatically increased (Fig. 6a and Movie S4, Supporting Information). The bursting pressure of the polysaccharide nanosheet reached 56.7 ± 6.1 cm H_2O at 3 h after repair. The mechanical strength of the polysaccharide nanosheet was probably reinforced by the deposition of blood cell components, such as erythrocytes and platelets within fibrin networks, as seen in Figure 3b. As this deposition occurs relatively quickly, the most significant increment in the mechanical strength was observed at 3 h after repair compared to that at 5 min, and it was not further increased at 24 h.

A further analysis of the wound healing after tissue-defect repair was undertaken by a histological examination for investigating the different healing mechanisms between the polysaccharide nanosheet and the fibrin sheet. Tissue specimens for histological

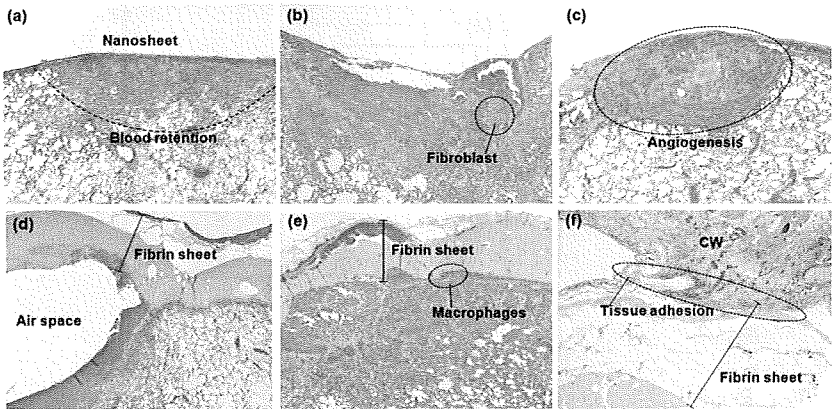

Figure 7. Representative histological findings at different time points after repair (hematoxylin–eosin staining, magnification 4×) using the polysaccharide nanosheet or the fibrin sheet. Upper and lower panels correspond to the polysaccharide nanosheet and the fibrin sheet, respectively, at 3 h (a, d), 3 days (b, e) and 7 days (c, f) after repair. At 7 days, angiogenesis occurred in the polysaccharide nanosheet groups while strong adhesion between the fibrin sheet and the chest wall (CW) was observed.

examination were obtained at 5 min, 3 h, 3 days, and 7 days after repair. The specimen containing the repairing lesion in each lobe was fixed with formalin followed by paraffinization and then stained with hematoxylin–eosin. It is noteworthy that the wound healing after treatment with the polysaccharide nanosheet was quite distinct from that with the fibrin sheet. Although it was difficult to observe the polysaccharide nanosheet overlapped on the pleural defect, the formation of flat-shaped blood clots localized along the polysaccharide nanosheet was clearly observed in the region of the defects at 5 min and 3 h after repair without significant inflammatory response, such as emergence of giant cells (Fig. 7a and S5, Supporting Information). This finding suggested that blood cells initially deposited under the polysaccharide nanosheet, as in the image of Figure 3b, were transformed to stable blood clots by persistent blood discharge from alveolar capillaries without blood clotting on the outside of the attached nanosheet. At 3 days after repair, fibroblasts were grown around the blood clots replacing the preformed clots (Fig. 7b). At 7 days after repair, angiogenesis was observed, in which the blood clots originally formed under the polysaccharide nanosheet, and any sequence of the wound healing process was never found on the outside of the polysaccharide nanosheet (Fig. 7c), resulting in no occurrence of postsurgical adhesive lesion in the thoracic cavity. At 30 days after repair, the original tissue-defect site was no longer confirmed. Following these findings, we found that the polysaccharide nanosheet worked not only as an interfacial separator between the in- and outside of the pleura, but also provided the flat and stable scaffold for the wound healing process.

In contrast to the polysaccharide nanosheet, repair of the pleural defect by the fibrin sheet exhibited large vacant air spaces at 3 h because the thick fibrin sheet was not so flexible to densely overlap the defect site. This caused detachment from the lesion of the pleural defect due to an influx of discharge into the air space between the pleura and the fibrin sheet (Fig. 7d), resulting in the random retention of blood components in the overlapped area. At 3 days, the random growth of fibroblasts was observed as well as the induction of inflammatory tissue reaction, such as an emergence of macrophages (Fig. 7e). Furthermore, it is a critically important clinical issue that the fibrin sheet also strongly adhered onto the chest wall (Fig. 7f). Severe pleural adhesion might reduce a respiratory function and may cause a reoccurrence of pneumothorax. The polysaccharide nanosheet has very desirable properties: physical adhesiveness due to flexibility and sufficient mechanical strength without chemical and biological adhesives. Thus, repair by overlapping a tissue defect with the polysaccharide nanosheet has a significant advantage in maintaining the function of the remaining lung against sustained ventilation and the pressure from respiration and bleeding.

6. Conclusions

We succeeded in the construction of a free-standing polysaccharide nanosheet under totally aqueous conditions exploiting the SA-LbL method. Furthermore, we found that the polysaccharide nanosheet with a thickness of 75 nm was suitable for repairing a visceral pleural defect without any loss of respiratory functions of the lung, as determined by a bulge test and in vivo study. We utilized the flexible properties of the soft nano-biomaterial built from secondary interactions for a minimally invasive treatment of the tissue-defect repair without postsurgical adhesion. The applications of polymer nanosheets are expected to include not only respiratory surgery, but also tissue repair of other organs. The desirable mechanical properties of the polymer nanosheet can be easily modulated by changing the polymer and thickness. Therefore, combination with other functionally biocompatible polymers will expand the applicability of the polymer nanosheet as a novel wound dressing of tissue-defect repair from soft to hard organs, which is currently being investigated in our group.

7. Experimental

Materials: The biodegradable polyelectrolytes, chitosan (molecular weight, $M_w = 88$ kDa) and Na Alginate ($M_w = 106$ kDa), were purchased from Nacalai Tesque, Inc. (Kyoto, Japan). PVA ($M_w = 22$ kDa) was purchased from Kanto Chemical Co., Inc. (Tokyo, Japan). Silicon wafers (SiO_2 substrates) purchased from KST World Co. (Fukui, Japan) were cut into a proper size (typically 4 cm^2), immersed in a mixture of sulfuric acid and hydrogen peroxide (3:1) for a 10 min wash, and then thoroughly rinsed with deionized (DI) water (18 MΩ cm).

Preparation and Characterization of the Polysaccharide Nanosheet: All preparation routines for polysaccharide nanosheet fabrication were conducted in a clean room (class 10 000 conditions) to avoid contamination. Chitosan (1 mg mL^{-1}, 1% (v/v) acetic acid) and Na alginate (1 mg mL^{-1}) solutions were prepared with DI water. A 1 mL solution of chitosan as a first layer was dropped onto the SiO_2 substrate,and then the substrate was rotated at 4500 rpm (rpm = revolutions per minute) for 15–20 s. Then, the substrate was rinsed twice with DI water and dried by spinning (~30 s). Then, nanosheets were prepared via the following steps: i) repetition of chitosan and Na alginate multilayering by a SA-LbL method (4500 rpm, 15 s for each polyelectrolyte) and rinsing by water after each

layering; ii) termination of SA-LbL in a chitosan spin-coating stage and drying the surface by N_2 flow; iii) casting of a supporting layer of a 10 wt% PVA aqueous solution on the polysaccharide multilayered substrate for over 12 h until the PVA film was dry; iv) peeling of the bilayered film of the polysaccharide nanosheet and PVA from the SiO_2 substrate using tweezers, so that it could be used for wound repair of beagle dogs. Another such bilayered film was immersed in water or PBS (pH 7.4) in order to obtain the polysaccharide nanosheet, which was then scooped onto a bare SiO_2 or PP substrate. Then the polysaccharide nanosheet on the substrate was left until the water was aspirated in a desiccator. The surface morphology, such as thickness and RMS roughness, was analyzed by an α-step surface profiler (KLA-Tencor Corp., San Jose, CA), and the overall morphology of the polysaccharide nanosheet was photographed using an OLYMPUS C-5050 ZOOM digital camera (Olympus Co., Tokyo, Japan). The SEM observation of the polysaccharide nanosheets was undertaken with a HITACHI S-4300 at an accelerating voltage of 10 kV, using samples on a porous alumina membrane (Anodisc, Whatman Ltd., Maidstone, UK) coated with a platinum layer (~5 nm thickness) using an ion-sputtering coater HITACHI E-1045 (Hitachi Ltd., Tokyo, Japan).

SEM Observation of the Polysaccharide Nanosheet in Contact With Blood: Blood (2 μL, donated from T. F. with his permission) mixed with a tenfold volume of 3.8% (w/v) sodium citrate was dropped on the surface of a polysaccharide nanosheet which covered an albumin-adsorbed PP prefilter (30 μm porous filter: Millipore Co., Billerica, MA). The sample was fixed with 1% (v/v) glutaraldehyde in 0.1 M phosphate buffer (pH 7.4) for 30 min, postfixed with 1% (w/v) osmium tetroxide in the same buffer for 30 min, and dehydrated with a graded ethanol series. After drying the sample in a Hitachi ES-2020 freeze-dryer using *t*-butyl alcohol, SEM observation was undertaken using a HITACHI S-4500 at an accelerating voltage of 10 kV, where the sample on the filter was coated with an osmium tetroxide layer (~30 nm thickness) using an NL-OPC80 ion-sputtering coater (Nippon Laser & Electronics Lab, Nagoya, Japan).

Evaluation of Physical Adhesive Properties: The micro-scratch tester (CSR-2000, Rhesca Co., Tokyo, Japan) was utilized for evaluation of the physical adhesive properties of the polysaccharide nanosheet. We prepared nanosheets of various thicknesses ranging from 39 to 1482 nm. The micro-scratch tester employs a diamond stylus of 25 μm in radius, and the stylus is forced to oscillate with an amplitude of 100 μm parallel to the surface of the polysaccharide nanosheets adhered onto the SiO_2 substrate, where the adhesive failure of the nanosheet peeled by the stylus was detected as a critical load of the polysaccharide nanosheet.

Evaluation of Mechanical Properties: The bulge test was used for evaluation of the mechanical strength of the polysaccharide nanosheets. A free-standing polysaccharide nanosheet floating in water was scooped onto a steel plate, where either a 1 or 6 mm diameter circular hole was made in the middle. The plate covered with the polysaccharide nanosheet was then fixed onto a custom-made steel chamber by firm adhesion. The pressure applied to the polysaccharide nanosheet through the circular hole of the plate was monitored by a digital pressure gauge (Keyence Co., Tokyo, Japan), and the deflection of the polysaccharide nanosheet was viewed from the side by a stereomicroscope (Olympus Co., Tokyo, Japan) until distortion was apparent. Each measurement for a polysaccharide nanosheet of a particular thickness was performed at least three times. In order to determine the ultimate tensile strength, the ultimate tensile elongation, and the elastic modulus of the polysaccharide nanosheets, the following equations were used:

$$\sigma = \frac{P \times a^2}{4 \times h \times d} \quad (1)$$

$$\varepsilon = \frac{2 \times d^2}{3 \times a^2}, \qquad E = \frac{\sigma}{\varepsilon} \quad (2)$$

where σ, P, a, h, d, ε, and E represent tensile stress, applied pressure, radius of the circular hole of the steel plate, thickness, deflection, tensile strain, and elastic modulus about the polysaccharide nanosheet, respectively. A schematic diagram of the bulge test is shown in the Supporting Information.

Visceral Pleural Defect Repair: Twenty-four male beagle dogs weighing 10 kg on average were intubated after anesthesia with ketamine [10 mg kg^{-1}, intramuscular (i.m.)], pancuronium [0.1 mg kg^{-1}, intravenous (i.v.)], and sodium pentobarbital (25 mg kg^{-1}, i.v.). The cuffed endotracheal tube was connected to a mechanical respirator (Model SN-480-6, Shinano Inc., Tokyo, Japan), and the animals were ventilated with air (a tidal volume of 15 mL kg^{-1} and a respiratory rate of 10 times min^{-1}). The body temperature was stabilized at 39 °C by monitoring the rectal temperature. The dogs were placed in the left lateral position, and a right thoracotomy was performed. A pleural defect was made on the anterior, middle, and posterior surfaces of each lobe with the airway pressure maintained at 10 cm H_2O. The defect was a 6 mm circle with a depth of 2 mm using an aorta punch (Scanlan, St. Paul, MN, USA). Bleeding vessels were cauterized if needed, but sites where hemostasis was difficult to achieve were not used. The pleural defects were repaired using either the polysaccharide nanosheet or fibrin-glue-coated collagen fleece (i.e., fibrin sheet, TachoComb, CSL Behring, Tokyo, Japan). An 18 mm × 18 mm piece of each sheet was applied over the defect. At 5 min, 3 h, and 24 h after repair, pressure was applied from the airway, and the bursting pressure of the applied sheets was measured with a manometer (ADInstrument BPamp, Utah Medical Products Inc., UT). Histological specimens were also obtained from the dogs at 5 min, 3 h, 3 days, and 7days after repair. All data are shown as the mean ± SD. Statistical analyses were performed using an unpaired *t*-test with $p < 0.05$ set as the level of statistical significance. All animal experiments were approved by the Animal Research Committee of the National Defense Medical College.

Acknowledgements

The authors thank Dr. Hidenori Suzuki at the Center for Electron Microscopy, the Tokyo Metropolitan Institute of Medical Science and Assoc. Prof. Teruyuki Komatsu and Invited Researcher Lu Gang at the Research Institute for Science & Engineering, Waseda University for technical advice and useful discussions about SEM observations, and Rhesca Corporation for the micro-scratch test. This work was supported in part by the "High-Tech Research Center" Project for Waseda University: matching fund subsidy, Global COE "Practical Chemical Wisdom" (TF) and "Consolidated Research Institute for Advanced Science and Medical Care" (ST) from MEXT, and a grant-in-aid for the Special Research Program from the National Defense Medical College (NM and MK). TF was the "Doctor-21" scholar of the Yoshida Scholarship Foundation. YO was the recipient of Japan Health Sciences Foundation. Supporting Information is available online from Wiley InterScience or from the author.

Received: January 20, 2009
Revised: February 17, 2009
Published online: July 1, 2009

[1] C. Jiang, S. Markutsya, Y. Pikus, V. V. Tsukruk, *Nat. Mater.* **2004**, *3*, 721.
[2] C. Jiang, V. V. Tsukruk, *Adv. Mater.* **2006**, *18*, 829.
[3] S. S. Ono, G. Decher, *Nano Lett.* **2006**, *6*, 592.
[4] R. Vendamme, S. Onoue, A. Nakao, T. Kunitake, *Nat. Mater.* **2006**, *5*, 494.
[5] H. Endo, Y. Kado, M. Mitsuishi, T. Miyashita, *Macromolecules* **2006**, *39*, 5559.
[6] T. Fujie, Y. Okamura, S. Takeoka, *Adv. Mater.* **2007**, *19*, 3549.
[7] T. Fujie, Y. Okamura, S. Takeoka, *Colloids Surf. A* **2009**, *334*, 28.
[8] Y. Lvov, G. Decher, H. Möhwald, *Langmuir* **1993**, *9*, 481.
[9] G. Decher, *Science* **1997**, *277*, 1232.
[10] *Multilayer Thin Films* (Eds: G. Decher, J. B. Schlenhoff), Wiley-VCH, Weinheim, Germany **2003**.
[11] Z. Tang, Y. Wang, P. Podsiadlo, N. A. Kotov, *Adv. Mater.* **2006**, *18*, 3203.
[12] H. L. Porte, T. Jany, R. Akkad, M. Conti, P. A. Gillet, A. Guidat, A. J. Wurtz, *Ann. Thorac. Surg.* **2001**, *71*, 1618.

[13] M. Kawamura, M. Gika, Y. Izumi, H. Horinouchi, N. Shinya, M. Mukai, K. Kobayashi, *Eur. J. Cardiothorac. Surg.* **2005**, *28*, 39.
[14] M. Gika, M. Kawamura, Y. Izumi, K. Kobayashi, *Interact. Cardiovasc. Thorac. Surg.* **2007**, *6*, 12.
[15] J. Cho, K. Char, J. Hong, K. Lee, *Adv. Mater.* **2001**, *13*, 1076.
[16] C. Jiang, S. Markutsya, V. V. Tsukruk, *Adv. Mater.* **2004**, *16*, 157.
[17] J. S. Boateng, K. H. Matthews, H. N. Stevens, G. M. Eccleston, *J. Pharm. Sci.* **2008**, *97*, 2892.
[18] H. J. Kim, H. C. Lee, J. S. Oh, B. A. Shin, C. S. Oh, R. D. Park, K. S. Yang, C. S. Cho, *J. Biomater. Sci. Polym. Ed.* **1999**, *10*, 543.
[19] M. N. V. R. Kumar, R. A. A. Muzzarelli, C. Muzzarelli, H. Sashiwa, A. J. Domb, *Chem. Rev.* **2004**, *104*, 6017.
[20] H. M. Yi, L. Q. Wu, W. E. Bentley, R. Ghodssi, G. W. Rubloff, J. N. Culver, G. F. Payne, *Biomacromolecules* **2005**, *6*, 2881.
[21] I. Liao, A. C. A. Wan, E. K. F. Yim, K. W. Leong, *J. Controlled Release* **2005**, *104*, 347.
[22] A. D. Stroock, R. S. Kane, M. Weck, S. J. Metallo, G. M. Whitesides, *Langmuir* **2003**, *19*, 2466.
[23] J. A. Forrest, K. Dalnoki-Veress, J. R. Stevens, J. R. Dutcher, *Phys. Rev. Lett.* **1996**, *77*, 2002.
[24] T. Serizawa, M. Yamaguchi, T. Matsuyama, M. Akashi, *Biomacromolecules* **2000**, *1*, 306.
[25] T. Serizawa, M. Yamaguchi, M. Akashi, *Biomacromolecules* **2002**, *3*, 724.
[26] J. Seo, J. L. Lutkenhaus, J. Kim, P. T. Hammond, K. Char, *Langmuir* **2008**, *24*, 7995.
[27] E. K. F. Yim, I. Liao, K. W. Leong, *Tissue Eng.* **2007**, *13*, 423.
[28] Z. K. Baldwin, A. L. Spitzer, V. L. Ng, A. H. Harken, *Surgery* **2008**, *143*, 305.
[29] S. Baba, T. Midorikawa, T. Nakano, *Appl. Surf. Sci.* **1999**, *144*, 344.
[30] J. J. Vlassak, W. D. Nix, *J. Mater. Res.* **1992**, *7*, 3242.
[31] S. Markutsya, C. Jiang, Y. Pikus, V. V. Tsukruk, *Adv. Funct. Mater.* **2005**, *15*, 771.
[32] H. Watanabe, T. Ohzono, T. Kunitake, *Macromolecules* **2002**, *40*, 1369.
[33] A. J. Nolte, M. F. Rubner, R. E. Cohen, *Macromolecules* **2005**, *38*, 5367.
[34] C. Jiang, X. Wang, R. Gunawidjaja, Y.-H. Lin, M. K. Gupta, D. L. Kaplan, R. R. Naik, V. V. Tsukruk, *Adv. Funct. Mater.* **2007**, *17*, 2229.
[35] T. Fabian, J. A. Federico, R. B. Ponn, *Ann. Thorac. Surg.* **2003**, *75*, 1587.
[36] H. Miyamoto, T. Futagawa, Z. Wang, A. Yamazaki, A. Morio, S. Sonobe, H. Izumi, Y. Hosoda, E. Hata, *Jpn. J. Thorac. Cardiovasc. Surg.* **2003**, *51*, 232.
[37] P. Hollaus, N. Pridun, *J. Cardiovasc. Surg. (Torino)* **1994**, *35*, 169.

0090-9556/09/3711-2197–2203$20.00
DRUG METABOLISM AND DISPOSITION

DMD 37:2197–2203, 2009

Vol. 37, No. 11
28852/3523893
Printed in U.S.A.

Hemoglobin Vesicles, Polyethylene Glycol (PEG)ylated Liposomes Developed as a Red Blood Cell Substitute, Do Not Induce the Accelerated Blood Clearance Phenomenon in Mice

Kazuaki Taguchi, Yukino Urata, Makoto Anraku, Hiroshi Watanabe, Daisuke Kadowaki, Hiromi Sakai, Hirohisa Horinouchi, Koichi Kobayashi, Eishun Tsuchida, Toru Maruyama, and Masaki Otagiri

Department of Biopharmaceutics (K.T., Y.U., M.A., H.W., D.K., T.M., M.O.), Center for Clinical Pharmaceutical Sciences (H.W., D.K., T.M.), Graduate School of Pharmaceutical Sciences, Kumamoto University, Kumamoto, Japan; Faculty of Pharmaceutical Sciences, Sojo University, Kumamoto, Japan (M.O.); Research Institute for Science and Engineering, Waseda University, Tokyo, Japan (H.S., E.T.); and Department of Surgery, School of Medicine, Keio University, Tokyo, Japan (H.H., K.K.)

Received June 6, 2009; accepted August 10, 2009

ABSTRACT:

The hemoglobin vesicle (HbV) is an artificial oxygen carrier encapsulating a concentrated hemoglobin solution in a liposome of which the surface is covered with polyethylene glycol (PEG). It was recently reported that repeated injections of PEGylated liposomes induce the accelerated blood clearance (ABC) phenomenon, in which serum anti-PEG IgM plays an essential role. To examine this issue, we investigated whether HbV induces the ABC phenomenon in mice at a dose of 0.1 mg Hb/kg, a dose that is generally known to induce the ABC phenomenon, or at 1400 mg Hb/kg, which is proposed for clinical use. At 7 days after the first injection of nonlabeled HbV (0.1 mg Hb/kg), the mice received HbV in which the Hb had been labeled with ^{125}I. After a second injection, HbV was rapidly cleared from the circulation, and uptake clearances in liver and spleen were significantly increased. In contrast, at a dose of 1400 mg Hb/kg, the pharmacokinetics of HbV was negligibly affected by repeated injection. It is interesting to note that IgM against HbV was produced 7 days postinjection at both of the above doses, and their recognition site was determined to be 1,2-distearoyl-*sn*-glycero-3-phosphatidylethanolamine-*N*-PEG in HbV. These results suggest that a clinical dose of HbV does not induce the ABC phenomenon, and that suppression of ABC phenomenon is caused by the saturation of phagocytic processing by the mononuclear phagocyte system. Thus, we conclude that induction of the ABC phenomenon would not be an issue in the dose regimen used in clinical settings.

It is well known that liposomes are able to function as carriers of drugs (Noble et al., 2006) and genes (Tuffin et al., 2005), and they have the ability to enhance blood retention and to specifically target encapsulated materials because the cellular structure of such vesicles is able to protect encapsulated materials against degradation and enhance their biodistribution. Many liposome-type drugs such as AmBisome (Astellas Pharma US, Inc., Deerfield, IL) and Doxil (Ortho Biotech, Horsham, PA), which have been approved for use and are currently in clinical use, take advantage of these characteristics. There is now little doubt that liposomes are useful and are in widespread use. To further enhance the quality and efficiency of liposomes, they are frequently modified with polyethylene glycol (PEG) (Veronese and Pasut, 2005). PEGylated liposomes exhibit a prolonged half-life, a higher stability, are water-soluble, have lower immunogenicity and antigenicity, as well as the potential for specific cell targeting. Because of these attributes, the majority of the recently developed liposome formulations are modified with PEG (Sakai et al., 2008; Okamura et al., 2009).

However, Dams et al. (2000) and Ishida et al. (2003a) reported that the intravenous injection of PEGylated liposomes causes a second dose of liposomes to lose their long-circulating characteristics and accumulate extensively in the liver when they are administered twice in the same animal [referred to as the accelerated blood clearance (ABC) phenomenon]. In addition, based on reported liposomal pharmacokinetics data, it is clear that several factors (e.g., size, lipid composition, surface modification, and membrane fluidity) influence the circulating time and the distribution to targeting areas (Ishida et al., 2004; Samad et al., 2007). Ishida et al. (2004) showed that the

This work was supported in part by Health Sciences Research grants (Health Science Research including Drug Innovation) from the Ministry of Health, Labor, and Welfare, Japan.

Article, publication date, and citation information can be found at http://dmd.aspetjournals.org.

doi:10.1124/dmd.109.028852.

ABBREVIATIONS: PEG, polyethylene glycol; ABC, accelerated blood clearance; HbV, hemoglobin vesicle; Hb, hemoglobin; PLP, pyridoxal 5′-phosphate; MPS, mononuclear phagocyte system; DPPC, 1,2-dipalmitoyl-*sn*-glycero-3-phosphatidylcholine; DHSG, 1,5-bis-*O*-hexadecyl-*N*-succinyl-L-glutamate; DSPE-PEG, 1,2-distearoyl-*sn*-glycero-3-phosphatidylethanolamine-*N*-PEG; rHSA, recombinant human serum albumin; ^{125}I-HbV, ^{125}I-labeled hemoglobin vesicle; BSA, bovine serum albumin; ELISA, enzyme-linked immunosorbent assay; CL_{uptake}, uptake clearance; AUC, area under the concentration-time curve; CL, clearance.

physicochemical properties of liposomes, such as lipid composition, diameter, surface modification, and dose, can also have an effect on the ABC phenomenon. Moreover, they also found that anti-PEG IgM, produced by the spleen in response to an injected dose of PEGylated liposomes, is involved in the induction of the ABC phenomenon (Ishida et al., 2006a).

Hemoglobin vesicles (HbV) have been developed as a cellular type of oxygen carrier, in which highly concentrated hemoglobin (Hb) is encapsulated in a phospholipid bilayer membrane with PEG. There are some distinct advantages for HbV to exist in a liposomal structure; the oxygen affinity (P_{50}) of HbV can be easily regulated by manipulating the content of an allosteric effector such as pyridoxal 5′-phosphate (PLP) (Sakai and Tsuchida, 2007). Furthermore, the diameter of HbV liposomes can be tailored to approximately 250 nm, and further modification by PEG leads to an enhanced lifetime in the blood circulation compared with other types of hemoglobin-based oxygen carriers ($t_{1/2}$ for cell-free Hb and PEGylated Hb in rats of 1.5 and 10.9 h, respectively) (Goins et al., 1995; Lee et al., 2006) because the encapsulation of Hb completely suppresses renal excretion, although HbVs in the circulation are eventually captured by phagocytes in the mononuclear phagocyte system (MPS) (Sakai et al., 2001). In fact, our group reported that HbV has a long circulation time in blood as an oxygen carrier in mouse, rat, rabbit, and a hemorrhagic shock model rat (Sou et al., 2005; Taguchi et al., 2009a,b). Because of these unique characteristics, such liposomes show an oxygen transport comparable with red blood cells (Sakai et al., 2008) and also show improved survival in hemorrhagic shock animal models (Sakai et al., 2004b, 2009).

In clinical use, it is expected that repeated high-dose injections would be required, as a red blood cell substitute, in patients with massive hemorrhage. Therefore, the possibility remains that repeated injections of HbV could induce the ABC phenomenon in a clinical situation. If the ABC phenomenon were induced by repeated injections, then the pharmacological action of HbV could be influenced. Therefore, it becomes necessary to characterize the pharmacokinetic properties of HbV after repeated injections at a dose that is routinely used in clinical practice as a red blood cell substitute.

In this study, we investigated whether the first injection of HbV at a low dose (0.1 mg Hb/kg), in which the lipid dose induced the ABC phenomenon, as reported by Ishida et al. (2003a), or a high dose (1400 mg Hb/kg), a dose that is proposed for use in a clinical situation, affects the pharmacokinetic behavior of HbV after the second injection in mice. In addition, we also investigated whether anti-HbV IgM is produced after the first injection, and which lipid component of HbV is recognized by IgM.

Materials and Methods

Materials. An Hb solution, from outdated donated blood, was provided by the Japanese Red Cross Society (Tokyo, Japan) and purified according to a previously described purification method (Sakai et al., 2002). PLP was purchased from Sigma-Aldrich (St. Louis, MO). Powdered 1,2-dipalmitoyl-*sn*-glycero-3-phosphatidylcholine (DPPC), cholesterol, and 1,5-bis-*O*-hexadecyl-*N*-succinyl-L-glutamate (DHSG) were purchased from Nippon Fine Chemical (Osaka, Japan), and 1,2-distearoyl-*sn*-glycero-3- phosphatidylethanolamine-*N*-PEG (DSPE-PEG; molecular weight of PEG = 5000) was purchased from NOF Co. (Tokyo, Japan). Recombinant human serum albumin (rHSA) was a gift from Nipro Corp. (Osaka, Japan). Iodine-125 as $Na^{125}I$ was purchased from PerkinElmer Life and Analytical Sciences (Waltham, MA). Horseradish peroxidase-conjugated goat anti-mouse IgG (Cayman Chemical, Ann Arbor, MI) and peroxidase-labeled affinity purified antibody to mouse IgM (μ) were purchased from Sigma-Aldrich.

Preparation of HbVs. HbVs were prepared under sterile conditions, as previously reported (Sakai et al., 1997). A typical encapsulated Hb (38 g/dl) solution contained 14.7 mM PLP as an allosteric effector to regulate the P_{50} to 25 to 28 Torr. The lipid bilayer comprised a mixture of DPPC, cholesterol, and DHSG at a molar ratio of 5:5:1, and PEG-DSPE (0.3 mol%). The HbVs were suspended in a physiological saline solution at [Hb] 10 g/dl, filter-sterilized (Dismic; Toyo-Roshi, Tokyo, Japan; pore size, 450 nm), and bubbled with N_2 for storage. The content of lipopolysaccharide was <0.1 EU/ml.

HbV Labeling with ^{125}I. ^{125}I-labeled HbVs (^{125}I-HbVs) were prepared as previously reported (Taguchi et al., 2009a). In a typical preparation, ^{125}I-HbV was prepared by incubating HbV with $Na^{125}I$ in Iodo-Gen (1,3,4,6-tetrachoro-3α,6α-diphenylglycoluril) and was separated from free ^{125}I by passage through a PD-10 column (GE Healthcare, Little Chalfont, Buckinghamshire, UK). The ^{125}I-HbVs were then sterile-filtered (pore size, 450 nm) to remove aggregates. More than 97% of the iodine was bound to internal Hb in this HbV preparation. Before use in experiments, two different concentrations of ^{125}I-HbV suspensions were prepared by mixing with nonradiolabeled HbV to adjust the target Hb concentration (0.1 or 1400 mg Hb/kg). All the suspensions were mixed with rHSA to adjust the albumin concentration of the vesicle suspension medium to 5 g/dl. Under these conditions, the colloid osmotic pressure of the suspension was maintained constant at approximately 20 mm Hg (Sakai et al., 2004b).

The Pharmacokinetic Experimental Protocol. All of the animal experiments were performed according to the guidelines, principles, and procedures for the care and use of laboratory animals of Kumamoto University. All the mice were given water containing 5 mM sodium iodide (NaI) for the duration of the experiment to avoid any specific accumulation in the glandula thyreoidea. Male ddY mice (28–30 g; Japan SLC, Inc., Shizuoka, Japan) were anesthetized using ether and received a single injection of a nonlabeled HbV suspension (0.1 or 1400 mg Hb/kg, 420 μl/30 g) to the tail vein. Seven days after the first injection of the nonlabeled HbV suspension, the same ddY mice received a ^{125}I-HbV suspension to the tail vein under ether anesthesia (the concentration and injected volume were identical to those for the first injection). Each mouse received a total dose of 2×10^6 cpm/30 g ^{125}I activity. At each time after the injection of ^{125}I-HbV, blood was collected from the inferior vena cava under ether anesthesia, and plasma was separated by centrifugation (3000*g*, 5 min). One percent bovine serum albumin (BSA) and 40% trichloroacetic acid were added to the plasma to remove degraded protein and free ^{125}I, and pellets were obtained by centrifugation (1000*g*, 10 min). After collecting blood, the animal was sacrificed for excision of organs (kidney, liver, spleen, heart, and lung), which were rinsed with saline and weighed. ^{125}I radioactivity in the plasma and excised organs was determined using a liquid scintillation counter (ARC-5000; Aloka, Tokyo, Japan).

Quantitative Determination of Anti-HbV IgG and IgM. The ddY mice received injections of saline or HbV (0.1 or 1400 mg Hb/kg, 420 μl/30 g b.wt.) to the tail vein under ether anesthesia. At each time point (days 3, 7, and 10) after injection, blood was collected from the inferior vena cava. Plasma was collected after centrifugation (3000*g*, 5 min), and the supernatant was subsequently ultracentrifuged to remove intact HbV (50,000*g*, 30 min) (Sakai et al., 2003). The supernatant collected as the plasma sample and was stored at −80°C until used.

Enzyme-linked immunosorbent assay (ELISA) was used to detect IgG and IgM against HbV using a previously described method, with minor modifications (Wang et al., 2007). The empty vesicles, which contained 475 ng/ml lipids as HbV (comprising DPPC, cholesterol, DHSG, PEG-DSPE at a molar ratio of 5:5:1:0.3) were added to 96-well plates (Immuno 96 MicroWell Plate; Nalge Nunc International, Rochester, NY). The plates were incubated for 2 h at 25°C. After incubation, the wells were washed three times with a wash solution (50 mM Tris, 0.14 M NaCl, 0.05% Tween 20, pH 8.0). A blocking solution (50 mM Tris, 0.14 M NaCl, 1% BSA, pH 8.0) was then added to each well, and the plate was incubated for 2 h at 25°C. After incubation, the wells were washed three times with wash solution, and 100 μl of plasma sample, diluted 1:100 with sample solution (50 mM Tris, 0.14 M NaCl, 0.05% Tween 20, 1% BSA, pH 8.0), was added to the wells. After incubation for 90 min, the wells were washed three times with wash solution, and 100 μl of horseradish peroxidase-conjugated goat anti-mouse IgG or peroxidase-labeled affinity purified antibody to mouse IgM (μ), diluted 1:1000 with sample solution, was added to each well. After incubation for 60 min, the wells were washed three times with wash solution. Coloration was initiated by adding 100 μl of *o*-phenylene diamine (1 mg/ml). After incubation, the reaction was terminated